Ore Geology Reviews 91 (2017) 216–235

Contents lists available at ScienceDirect

Ore Geology Reviews

journal homepage: www.elsevier.com/locate/oregeorev

Geology and geochemistry of the Jianchaling hydrothermal nickel deposit: T–pH–fO_2–fS_2 conditions and nickel precipitation mechanism

Jiuyang Jiang, Yongfeng Zhu*

The Key Laboratory of Orogenic Belts and Crustal Evolution, Ministry of Education, China
School of Earth and Space Sciences, Peking University, Beijing 100871, China

ARTICLE INFO

Keywords:
Hydrothermal nickel deposit
Serpentinite
Talc–carbonate rocks
Jianchaling

ABSTRACT

The Jianchaling nickel deposit in the Bikou Terrane (Shaanxi Province, China) occurs along the boundaries between granite porphyry and carbonated ultramafic rocks (carbonated serpentinite, talc–carbonate rocks, and listwaenite). Serpentine– magnetite, serpentine– magnesite– magnetite, and magnesite– talc– quartz– pyrite– violarite– millerite– chalcopyrite assemblage formed in carbonated ultramafic rocks during hydrothermal activities. Ni-bearing sulphides, coexisting with magnesite, postdated magnetite in carbonated ultramafic rocks. Compared with serpentinite, Ni, Co, Cu, Mn, and Pb concentrate in talc–carbonate rocks. The fact that the NiO contents of magnetite decrease with progressive carbonation of serpentinite suggests that Ni from magnetite concentrated in fluid and contributed to the formation of the Jianchaling nickel deposit. Sulphides precipitated from fluid with log fO_2 value varying from −34.5 to −31.8 and log fS_2 value varying from −10.3 to −9.2. High pH and HS^- activities triggered by transformation of serpentine into magnesite–talc–quartz assemblage promoted precipitation of Ni-bearing sulphides, and finally formed the Jianchaling hydrothermal nickel deposit.

1. Introduction

Hydrothermal nickel deposits, mainly hosted in mafic–ultramafic complexes (Keays and Jowitt, 2013; González-Álvarez et al., 2013a; Melekestseva et al., 2013) or black shale (Loukola-Ruskeeniemi and Lahtinen, 2013; Xu et al., 2013), are generally controlled by alteration zones or foliation fabrics. Nickel is present in millerite, violarite, and chlorite, and positive correlations between Ni and elements transported in hydrothermal fluids including Au and U are usually observed in hydrothermal nickel deposits. In contrast, magmatic nickel deposits generally occur at the base of their associated mafic–ultramafic bodies, with downward sulphide melt infiltration into floor rocks. Intercumulus sulphide blebs are composed mainly of pentlandite and pyrrhotite in magmatic nickel deposit, and Ni usually shows negative correlations with rare earth elements (REE) within mafic–ultramafic igneous system (Naldrett, 2004; Keays and Jowitt, 2013; Barnes et al., 2016). However, mineral assemblages formed during the re-equilibration and in-situ hydrothermal alteration in magmatic sulphide deposits are generally similar to sulphides crystallized in hydrothermal fluids (Barnes et al., 2009; Le Vaillant et al., 2016), and it is a challenge to distinguish a hydrothermal nickel ore-forming system from a magmatic one (González-Álvarez et al., 2013b). For example, the Epoch nickel deposit in Zimbabwe was improperly classified as a magmatic ore system, and it has been proven to be a hydrothermal nickel deposit (Pirajno and González-Álvarez, 2013). Similarly, the Jianchaling nickel deposit was once considered to be a magmatic one based on exsolution textures in pyrrhotite–pentlandite assemblage (Zhang et al., 1986; Wang et al., 2005). However, Jiang et al. (2010) suggests that it should be a hydrothermal deposit based on new data including the observations of Ni-bearing sulphides postdating igneous minerals. In fact, there are two types of ores with different sulphide assemblages in the Jianchaling nickel deposit: high-grade ores and low-grade ores. This study focused on the low-grade ores in the Jianchaling nickel deposit. We provide new petrology and geochemical data and phase equilibrium analysis to illustrate the hydrothermal ore-forming process in the Jianchaling nickel deposit.

2. Geological setting

Separated from the South Qinling Orogen by the Mianlue Suture Zone (Fig. 1a), the Bikou Terrane consists mainly of four geological units from bottom to top (Fig. 1b). The Neoarchean Yudongzi Group consists mainly of amphibolite and granitic gneiss with U–Pb ages of 2703–2645 Ma (Zhang et al., 2001, 2010). The Neoproterozoic Bikou Group consists mainly of basalt, andesite, tuff, sandstone, turbidite, slate, and phyllite. Neoproterozoic sedimentary rocks consist mainly of

* Corresponding author.
E-mail addresses: yfzhu@pku.edu.cn, jyjiang@pku.edu.cn (Y. Zhu).

http://dx.doi.org/10.1016/j.oregeorev.2017.10.005
Received 21 April 2017; Received in revised form 11 August 2017; Accepted 9 October 2017
Available online 10 October 2017

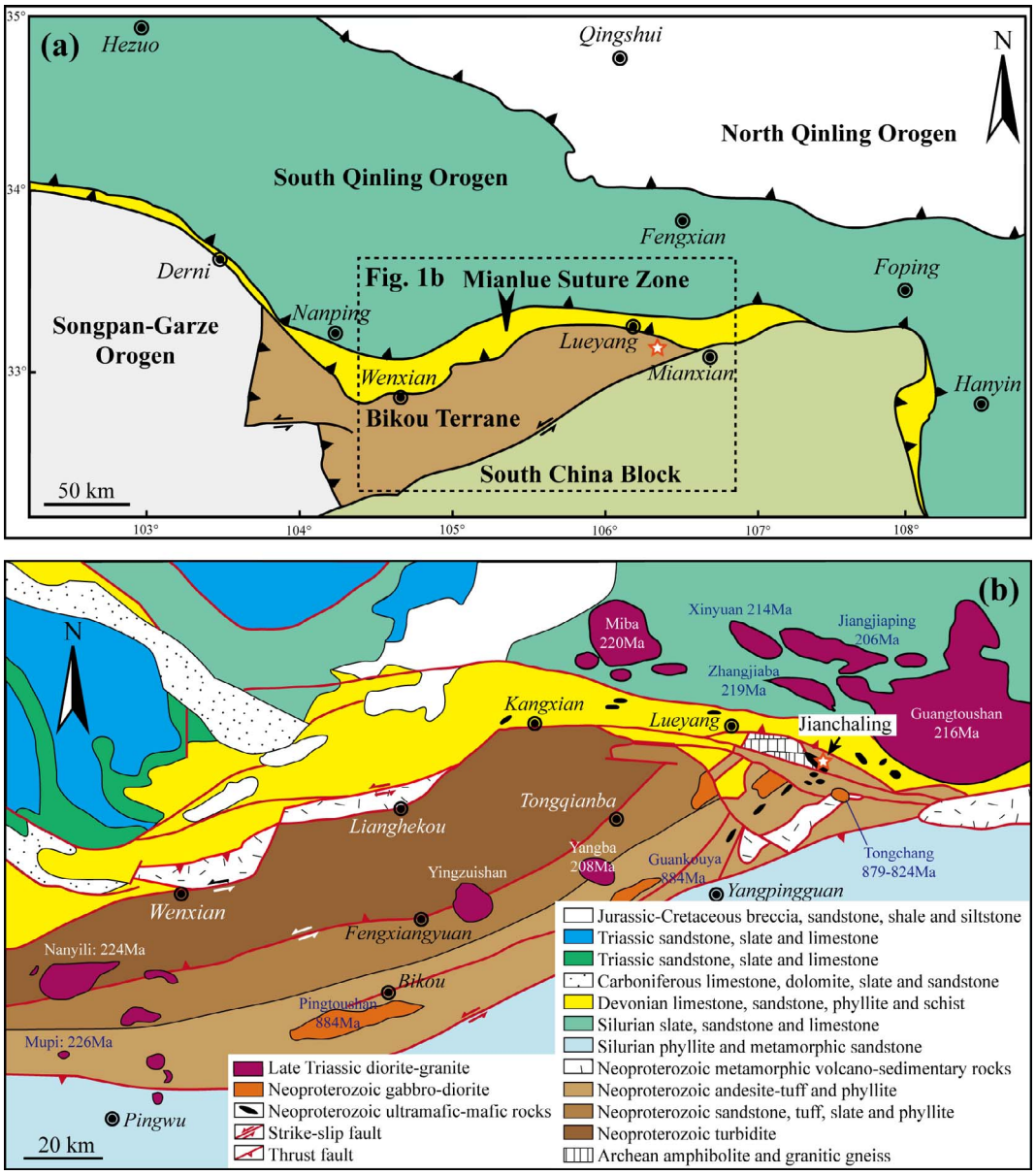

Fig. 1. (a) The Bikou Terrane and its adjacent tectonic units. (b) Geology map of the Bikou Terrane showing the distribution of sedimentary rocks, igneous rocks, and the Jianchaling nickel deposit (modified from Xia et al., 2007; Yang et al., 2015). Ages of the igneous rocks are cited from references (Sun et al., 2002; Zhang et al., 2007; Xiao et al., 2007; Lu et al., 2010; Wang et al., 2012; Yang et al., 2015).

dolomite, limestone, greywacke, conglomerate, slate, and phyllite. Devonian sedimentary rocks, composed mainly of limestone, sandstone, conglomerate, greywacke, and slate, unconformably cover the Neoproterozoic strata. The Pingtoushan diorite (884 ± 5.5 Ma), the Guankouya diorite (884 ± 14 Ma, Xiao et al., 2007), and the Tongchang diorite–granodiorite (879–824 Ma, Wang et al., 2012) intruded into the Yudongzi Group and the Bikou Group. Widespread intermediate–felsic intrusions emplaced into the Bikou Terrane and the South Qinling Orogen following the closure of the Mianlue Ocean during late Triassic (Zhang et al., 2007; Lu et al., 2010; Yang et al., 2015).

Several Proterozoic ultramafic suites in the Bikou Terrane occur along fault zones. Rocks from the Jianchaling ultramafic suite have a higher Ni grade (up to 3.72 wt%, Wang et al., 2005) compared with rocks from other ultramafic suites (Ni grade up to 1.30 wt%, Hou, 1992). The Jianchaling nickel deposit is the only nickel deposit mined in this region.

3. Geology of the Jianchaling nickel deposit

The Jianchaling nickel deposit is located in the Jianchaling ultramafic suite on the north margin of the Bikou Terrane (Fig. 1b). It has a resource of 2.20×10^5 tonnes of 0.57 wt% Ni and 1.0×10^4 tonnes of 0.026 wt% Co (Wang et al., 2003). The deposit was discovered by No. 711 Team of the Northwest Nonferrous Geo-exploration Bureau in 1970, and it was not mined until 2013 due to low grades of ores. The

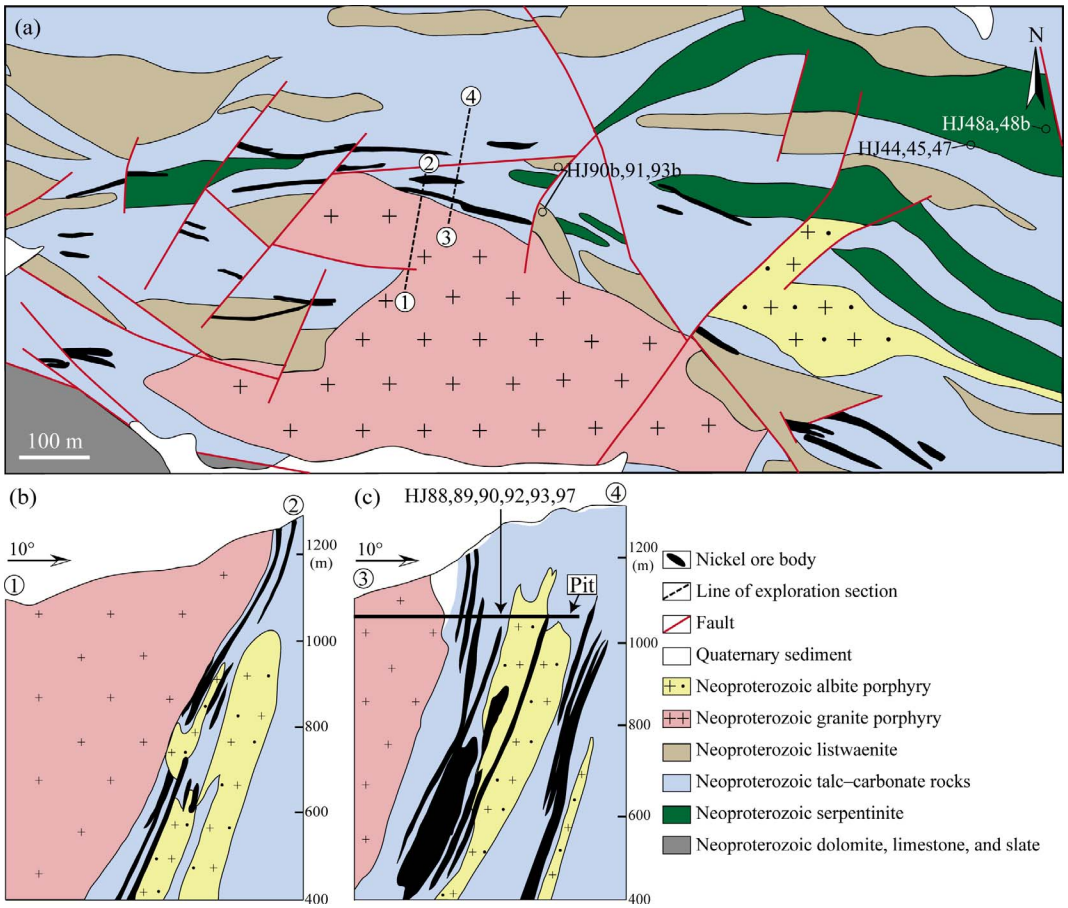

Fig. 2. (a) Geologic map of the Jianchaling nickel deposit and the exploration sections. (b) Vertical cross sections of the Jianchaling nickel deposit at Exploration Line 44 and (c) at Exploration Line 40 (modified from Wang et al., 1996; Li et al., 2014). Spatial distribution of sampling points are shown in the geologic map and cross section.

Jianchaling ultramafic suite, mainly composed of serpentinite, talc–carbonate rocks, listwaenite, and chlorite schist lenses, is 5.0 km in length and 0.3–1.0 km in width. Granite porphyry and albite porphyry intrusions, with zircon U–Pb ages of 844–859 Ma (Dai et al., 2014), emplaced into the ultramafic suite, dolomite, limestone, and sulphide-bearing slate (Fig. 2a). Ore bodies are distributed along the boundaries between carbonated ultramafic rocks and granite porphyry intrusions. Ni-bearing sulphide veins cut through albite porphyry intrusions. Different ore bodies measure 200–890 meters in length, 2–700 meters in depth, and 2–12 meters in thickness. These ore bodies dip to the south at 68–75°. Tabular ore bodies and ore lenses in the carbonated ultramafic rocks are thick in the deep part and thin in the shallow part (Fig. 2b–c). High-grade ores (> 1 wt% Ni) are hosted in serpentinite, chlorite–tremolite rocks, talc–carbonate rocks, and listwaenite. Low-grade ores (0.2–1.0 wt% Ni), accounting for 70% of the nickel resources in the Jianchaling nickel deposit, are hosted in talc–carbonate rocks and listwaenite. The boundaries between ore bodies and their wall-rocks are based on Ni contents.

Serpentinite (Fig. 3a) was transformed into carbonated serpentinite (Fig. 3b), talc–carbonate rocks (Fig. 3c–d), and finally listwaenite. Serpentinite is composed principally of serpentine (> 90 vol%) with trace amounts of magnesite and Cr-spinel. Some magnetite coexists with serpentine, while other magnetite coexists with magnesite (Fig. 4a).

Carbonated serpentinite is composed of serpentine (50–60 vol%), magnesite (25–30 vol%), talc (< 5 vol%), and trace amounts of Cr-spinel, dolomite, apatite, and monazite. Talc and magnesite replaced serpentine with unclear and curved boundaries (Fig. 4b). Fine-grained magnesite, magnesite veinlets, and medium-grained magnesite sequentially crystallized and replaced serpentine (Fig. 4c). Disseminated magnetite (5–10 vol%) and sulphides (< 5 vol%) occur in carbonated serpentinite (Fig. 3b and Fig. 4c).

Talc–carbonate rocks consist mainly of magnesite (60–65 vol%), talc (20–25 vol%), quartz (5–10 vol%), and trace amounts of Cr-spinel, dolomite, apatite, monazite, and chlorite. Magnesite coexists with talc and quartz (Fig. 4d–e). Disseminated magnetite (5–20 vol%) and sulphides (5–15l%) occur in talc–carbonate rocks (Fig. 3c–d, Fig. 4d–e).

Listwaenite consists mainly of magnesite (50–55 vol%), quartz (20–25 vol%), talc (5–10 vol%) (Fig. 4f), and trace amounts of Cr-spinel, dolomite, apatite, monazite, and chlorite. Disseminated magnetite (5–20 vol%) and sulphides (5–15 vol%) occur in listwaenite. Listwaenite is weakly deformed and locally sheared. Magnesite, quartz, magnetite, and sulphides occur along foliation fabrics of listwaenite.

Cr-spinel occurs in serpentinite, carbonated serpentinite, talc–magnesite rocks, and listwaenite. Chromite replaced Cr-spinel along fractures and rims (Fig. 5a–d). Cr-bearing magnetite occurs as veinlets crosscutting chromite or as alteration rims of chromite in serpentinite (Fig. 5a). Cr-bearing magnetite exists as alteration rims of chromite in

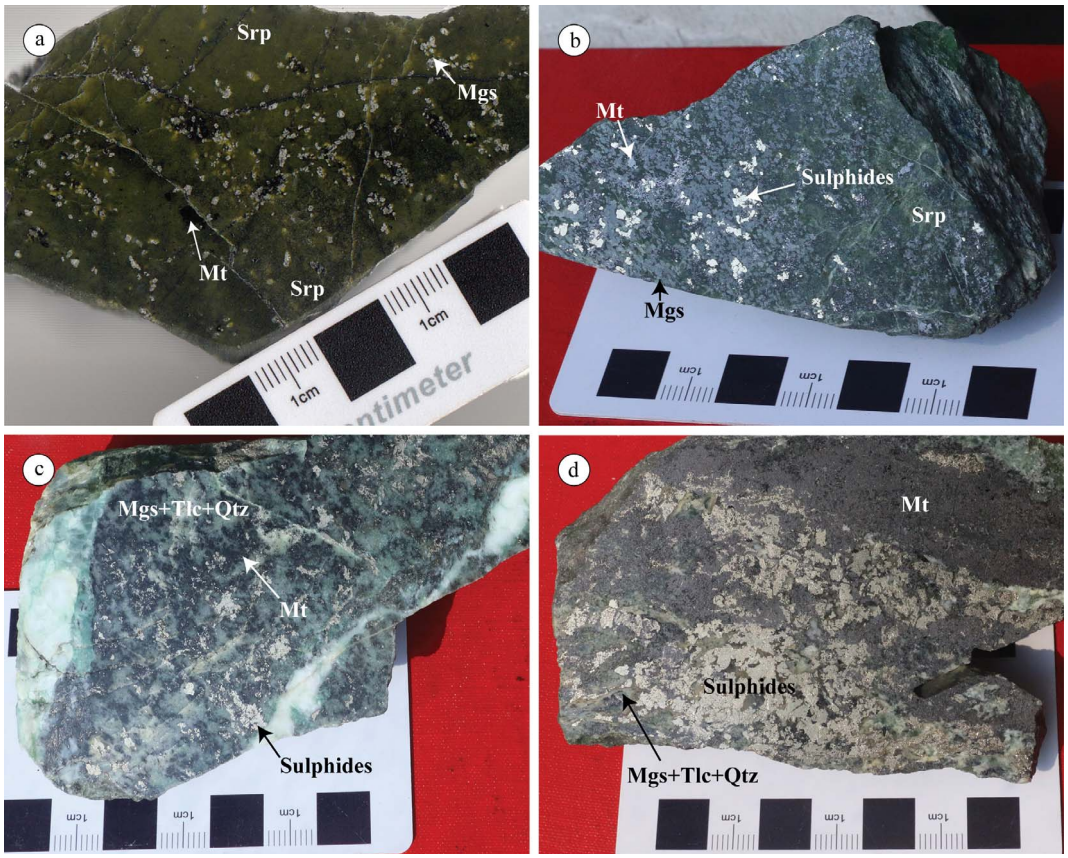

Fig. 3. Photographs showing serpentinite, carbonated serpentinite, and talc–carbonate rocks in the Jianchaling nickel deposit. (a) Trace amounts of magnesite and magnetite in serpentinite. (b) Disseminated sulphides in carbonated serpentinite. (c–d) Disseminated sulphides and magnetite in talc–carbonate rocks. Mgs – magnesite, Mt – magnetite, Qtz – quartz, Srp – serpentine, and Tlc – talc.

carbonated serpentinite (Fig. 5b), talc–carbonate rocks (Fig. 5c–d), and listwaenite.

The Cr# ($=100 \times Cr/(Cr + Al + Fe^{3+})$) of Cr-spinel ranges from 62.0 to 66.9 in serpentinite and talc–carbonate rocks, while the Mg# ($=100 \times Mg/(Mg + Fe^{2+})$) of Cr-spinel is highly variable (Table 1 and Table 2). Mg# of Cr-spinel in talc–carbonate rocks (6.0–51.6) is lower than Mg# of Cr-spinel in serpentinite (54.8–77.3, Fig. 5e). Cr-spinel in serpentinite and talc–carbonate rocks contains ≤ 2.46 wt% MnO. Chromite in talc–carbonate rocks contains lower MgO (≤0.09 wt%) and MnO (0.21–0.34 wt%) than that in serpentinite (4.53–12.01 wt% MgO, 5.95–7.89 wt% MnO). Cr-bearing magnetite contains 0.21–6.96 wt% Cr_2O_3. Cr-bearing magnetite in talc–carbonate rocks contains lower MgO (≤0.04 wt%) and MnO (≤0.12 wt%) than that in serpentinite (1.44–1.66 wt% MgO, 0.47–0.74 wt% MnO). NiO contents of Cr-bearing magnetite in serpentinite and talc–carbonate rocks range from 0.24 to 0.87 wt%, higher than those of Cr-spinel (≤0.09 wt%) and chromite (≤0.43 wt%).

Chlorite schist lenses are composed principally of chlorite and cummingtonite, with trace amounts of ilmenite, apatite, monazite, and thorite. Sulphide–dolomite veins crosscut chlorite schist (Fig. 6a). Pentlandite coexists with pyrrhotite, chalcopyrite, and Fe-bearing siegenite ($(Co, Ni, Fe)_3S_4$) in these veins (Fig. 6b). Cr-spinel is not present in chlorite schist, and metasomatic assemblage in chlorite schist is different from that in serpentinite, talc–carbonate rocks, and listwaenite. Therefore, the parental rock of chlorite schist is different from that of serpentinite. Sulphides occur in dolomite veins in chlorite schist, whereas disseminated sulphides occur in carbonated serpentinite, talc–carbonate rocks, and listwaenite. The sulphide–dolomite veins in chlorite schist represent a different style of Ni mineralization in wallrocks during carbonation process.

4. Analytical methods

Polished thin sections were prepared for backscattered electron imaging (BSE) analysis and electron probe microanalysis (EPMA). Oxide and silicate phases were analysed using a JXA-8230 electron microprobe, and sulphide phases were analysed using a JXA-8100 electron microprobe at Peking University. Analysis used a wavelength-dispersive X-ray detection system (WDS) with four crystal spectrometers. A run designed for oxide–silicate analysis and a run designed for sulphide analysis were used. Ten-second counting time was adopted for measurement of characteristic peak intensities and 5 s at each of the background positions at either side of the peak for the runs. The oxide–silicate run determined concentrations of Ca (K_α), Ti (K_α), Mg (K_α), Al (K_α), Cr (K_α), Mn (K_α), Fe (K_α), Ni (K_α), and Si (K_α), using an electron beam current of 10 nA and accelerating voltage of 15 kV with a beam diameter of 2 μm. The PRZ correction method was used for oxide–silicate standardization. The sulphide run determined concentrations of Fe (K_α), Se (L_α), As (L_α), S (K_α), Co (K_α), Sb (L_α), Ni (K_α), Te (L_α), Cu (K_α), and Zn (K_α), using an electron beam current of 10 nA and accelerating voltage of 20 kV with a beam diameter of 2 μm. The ZAF correction method was used for sulphide standardization.

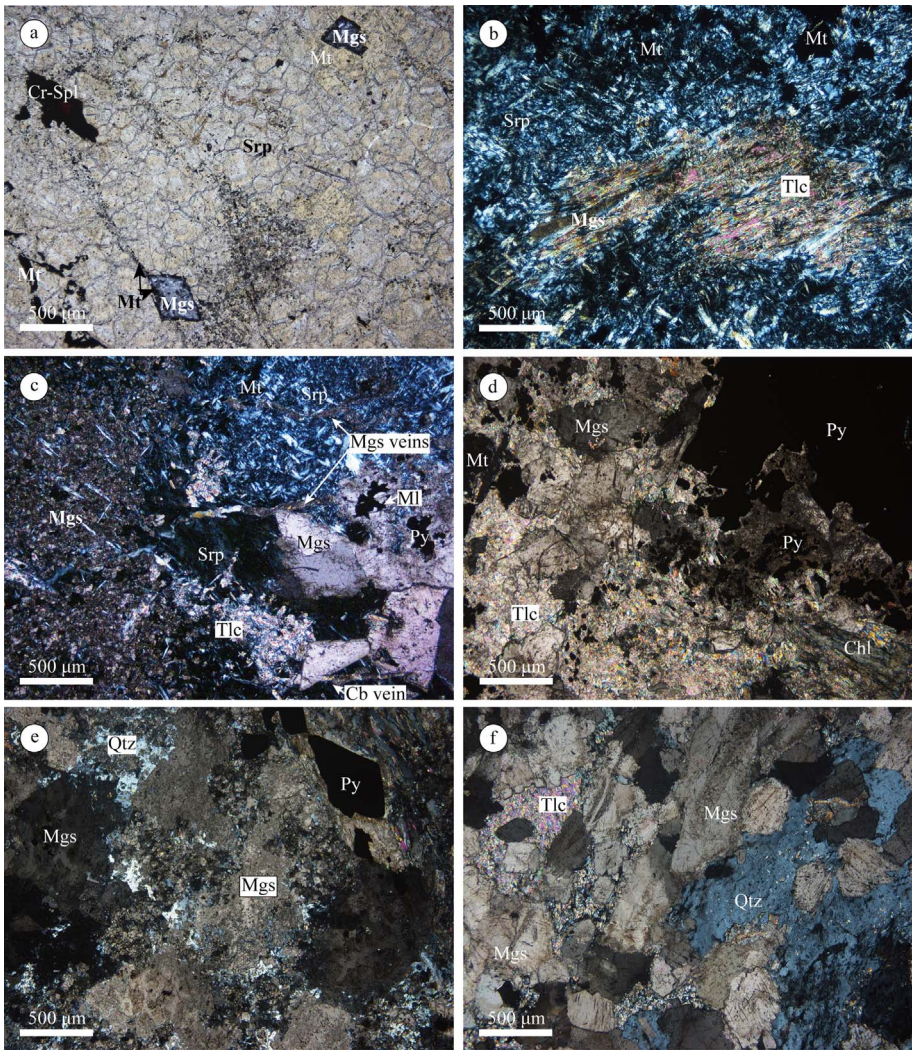

Fig. 4. Photomicrographs showing mineral assemblages in the Jianchaling ultramafic suite. (a) Trace amounts of magnesite and magnetite in serpentinite, plane-polarized light. (b) Magnesite and talc replacing serpentine in carbonated serpentinite. (c) Fine-grained magnesite, magnesite veinlets, and medium-grained magnesite in carbonated serpentinite. (d) Talc–carbonate rocks consisting mainly of magnesite and talc. (e) Quartz in talc–carbonate rocks. (f) Listwaenite consisting mainly of magnesite, quartz, and talc. b–f, cross-polarized light. Cr-Spl – Cr-spinel, Mgs – magnesite, Mt – magnetite, Py – pyrite, Qtz – quartz, Srp – serpentine, and Tlc – talc.

Talc–carbonate rocks (including low-grade ores) were collected from the pit along Exploration Line 40, while samples of serpentinite, carbonated serpentinite, and listwaenite were collected from outcrops in the ore district (Fig. 2) for trace elements analysis. The samples were washed by distilled water, and smashed to about 250 μm in size after being dried out. They were then ground to 75 μm in an agate mill. We weighed out 250 mg of powder for each sample, and digested it with $HClO_4$–HNO_3–HF (100 °C, 24 h, once) and aqua regia (50 °C, 24 h, twice) in a closed Teflon bottle. Each sample in a state of wet salt was finally diluted with 5 wt% HNO_3 to 25 mL, and was analysed using Agilent 7500 inductively coupled plasma-mass spectrometry (ICP-MS) at Peking University. The measurement precisions were 10% for all elements. Nickel concentrations were also analysed with atomic absorption spectroscopy.

Thermodynamic properties of Fe–Ni–Cu sulphides and iron oxides are from Simon and Essene (1996) and Waldner (2009) to calculate their stability fields. Phase equilibrium calculations of the CH_4–CO_2 buffer and the HS^-–SO_4^{2-} buffer in the ore-forming system are calculated using the SUPCRT92 software with the slop98.dat database (Johnson et al., 1992).

5. Ore petrology

Magnetite coexists with serpentine or magnesite, while fine-grained to medium-grained sulphides only coexist with magnesite in carbonated serpentinite (Fig. 7a–c). Disseminated pyrite and millerite with irregular shapes are distributed within magnesite matrix, while chalcopyrite is enclosed in pyrite (Fig. 7d).

Disseminated pyrite–millerite–violarite–chalcopyrite (PMVC) assemblage and disseminated magnetite occur in talc–carbonate rocks (Fig. 8a). Talc–carbonate rocks contain more sulphides (5–15 vol%) than those in carbonated serpentinite (< 5 vol%), while there is no obvious change of magnetite content (5–20 vol%). Pyrite veins crosscut Cr-spinel–chromite–Cr-bearing magnetite assemblage (Fig. 8b). Anhedral pyrite grains fill interstitial gaps between magnetite, and they replaced magnetite (Fig. 8c–d). Relict magnetite is enclosed in subhedral pyrite (Fig. 8d). Magnetite coexists with apatite and monazite (Fig. 8e). Fe contents of magnesite are inhomogeneous in talc–carbonate rocks. High-Fe magnesite, which crosscuts magnesite, surrounds pyrite (Fig. 8e–f).

Magnesite–violarite veinlets fill in well-connected fractures of pyrite (Fig. 9a and c). Irregular intergrowth of violarite, millerite, and

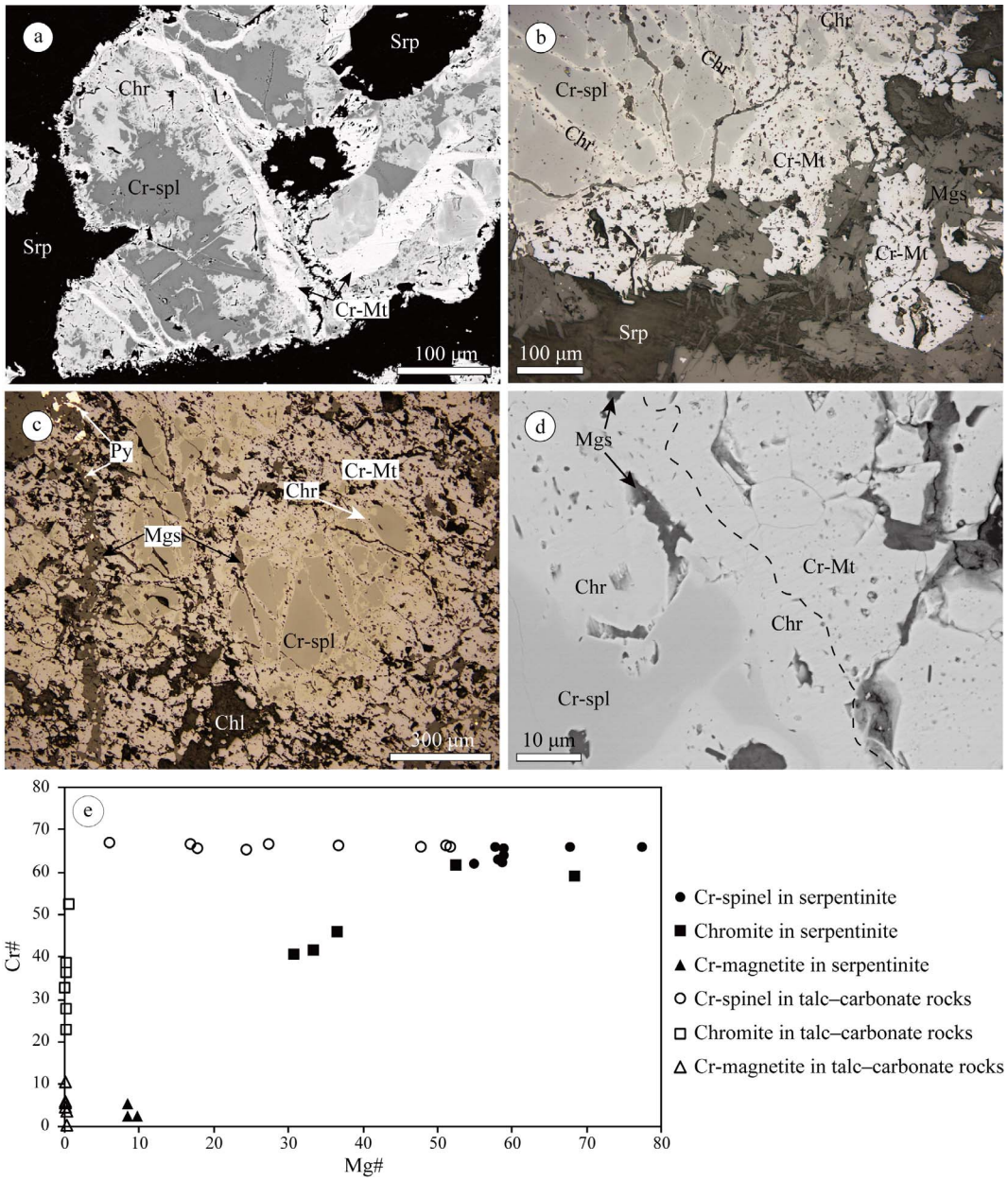

Fig. 5. Cr-spinel was replaced by chromite, and chromite was replaced by Cr-bearing magnetite in serpentinite (a, BSE), carbonated serpentinite (b, reflected light), and talc–carbonate rocks (c, reflected light; d, BSE). (e) Mg# (100 × Mg/(Mg + Fe^{2+})) versus Cr# (100 × Cr/(Cr + Al + Fe^{3+})) graph of Cr-spinel, chromite, and Cr-bearing magnetite in serpentinite and talc–carbonate rocks. Chl – chlorite, Chr – chromite, Cr-Mt – Cr-bearing magnetite, Cr-Spl – Cr-spinel, Mgs – magnesite, Py – pyrite, and Srp – serpentine.

magnesite fills interstitial gaps between pyrite (Fig. 9b). Violarite and millerite replaced pyrite from its rim (Fig. 9c). Some violarite and millerite replaced pyrite grains almost completely, where relict pyrite grains and magnetite grains are enclosed in millerite or violarite–millerite intergrowth (Fig. 9d–e). Violarite always coexists with millerite (Fig. 9b–d and f). High-Fe magnesite surrounds pyrite–violarite–millerite assemblage (Fig. 9 g).

Talc–carbonate rocks contain < 2 vol% chalcopyrite, far less than Fe–Ni sulphides (up to 15 vol%). Three kinds of chalcopyrite are identified: chalcopyrite inclusions within pyrite (Fig. 9c), chalcopyrite veinlets crosscutting pyrite (Fig. 9 h), and chalcopyrite coexisting with violarite and millerite (Fig. 9i).

Similar to that in talc–carbonate rocks, PMVC assemblage occurs in listwaenite. Disseminated sulphides postdated disseminated magnetite. High-Fe magnesite, crosscutting magnesite, surrounds pyrite (Fig. 10a). Pyrite, millerite, and violarite are distributed within magnesite matrix. The PMVC assemblage and magnetite are generally aligned along foliation fabrics of locally deformed listwaenite (Fig. 10b–f).

Cr-spinel is the only primary mineral in the serpentinite and carbonated ultramafic rocks. Cr-spinel was replaced by chromite, and chromite was replaced by Cr-bearing magnetite (Fig. 5a–d). Petrographic observations suggest that metasomatism in ultramafic rocks

Table 1
Representative compositions of Cr-spinel, chromite, and Cr-bearing magnetite in serpentinite by EPMA (in wt%, O = 4).

Mineral	Cr-spinel								Chromite						Cr-bearing magnetite		
SiO_2	bdl	bdl	bdl	bdl	bdl	bdl	bdl	bdl	bdl	bdl	bdl	bdl	bdl	bdl	bdl	bdl	bdl
TiO_2	bdl	bdl	bdl	bdl	bdl	bdl	bdl	bdl	bdl	bdl	bdl	bdl	bdl	bdl	bdl	bdl	bdl
Al_2O_3	18.19	17.92	18.10	19.75	17.93	19.08	18.91	19.48	0.25	11.81	0.04	bdl	0.09	bdl	bdl	bdl	bdl
Cr_2O_3	53.09	52.74	53.75	50.76	52.65	52.03	51.00	50.07	45.27	46.26	29.94	29.04	32.46	1.46	1.56	3.65
FeO^T	16.53	16.49	9.22	17.06	12.52	16.48	17.76	18.47	38.79	23.73	57.46	58.24	52.08	90.10	90.06	88.58
MnO	0.31	0.31	2.46	bdl	1.50	0.25	0.26	0.69	7.89	5.95	6.76	7.28	7.63	0.74	0.69	0.47
NiO	bdl	bdl	0.08	bdl	0.08	bdl	bdl	bdl	bdl	0.08	0.28	0.43	0.36	0.68	0.87	0.79
MgO	12.22	12.35	15.70	12.52	13.85	12.59	12.33	11.50	7.80	12.01	5.02	4.53	5.17	1.66	1.44	1.47
CaO	bdl	bdl	bdl	bdl	bdl	bdl	bdl	bdl	bdl	bdl	bdl	bdl	bdl	bdl	0.05	bdl
Total	100.42	99.92	99.37	100.56	98.63	100.50	100.31	100.27	100.05	99.99	99.56	99.65	97.83	94.72	94.75	95.08
Si	0	0	0	0	0	0	0	0	0	0	0	0	0	0	0	0
Ti	0	0	0	0	0	0	0	0	0	0	0	0	0	0	0	0
Al	0.671	0.664	0.659	0.721	0.665	0.699	0.695	0.719	0.010	0.447	0.002	0	0.004	0	0	0
Cr	1.315	1.311	1.312	1.244	1.310	1.279	1.258	1.239	1.236	1.174	0.833	0.810	0.919	0.043	0.046	0.108
Fe^{3+}	0.012	0.026	0.026	0.034	0.019	0.020	0.048	0.041	0.754	0.370	1.162	1.182	1.075	1.953	1.952	1.885
Fe^{2+}	0.421	0.408	0.212	0.408	0.311	0.409	0.416	0.443	0.366	0.267	0.529	0.536	0.483	0.864	0.867	0.882
Mn	0.008	0.008	0.064	0	0.040	0.007	0.007	0.018	0.231	0.162	0.201	0.217	0.231	0.023	0.022	0.015
Ni	0	0	0.002	0	0.002	0	0	0	0	0.002	0.008	0.012	0.010	0.020	0.026	0.024
Mg	0.571	0.579	0.723	0.579	0.650	0.584	0.574	0.537	0.401	0.575	0.263	0.238	0.276	0.093	0.080	0.082
Ca	0	0	0	0	0	0	0	0	0	0	0	0	0	0	0.002	0
Sum	3.000	3.000	3.000	3.000	3.000	3.000	3.000	3.000	3.000	3.000	3.000	3.000	3.000	3.000	3.000	3.000
$Cr/(Cr + Al + Fe^{3+})$	0.658	0.655	0.657	0.622	0.657	0.640	0.629	0.620	0.618	0.590	0.417	0.406	0.460	0.022	0.023	0.054
$Al/(Cr + Al + Fe^{3+})$	0.336	0.332	0.330	0.361	0.334	0.350	0.347	0.360	0.005	0.224	0.001	0	0.002	0	0.001	0.001
$Fe^{3+}/(Cr + Al + Fe^{3+})$	0.006	0.013	0.013	0.017	0.010	0.010	0.024	0.021	0.377	0.186	0.582	0.593	0.538	0.978	0.976	0.945
$Mg/(Mg + Fe^{2+})$	0.576	0.587	0.773	0.586	0.677	0.588	0.580	0.548	0.523	0.683	0.332	0.307	0.364	0.097	0.084	0.085

bdl = below detection limit.

and ore-forming process occurred in several stages (Fig. 11). Magnetite occurs in serpentinite and carbonated ultramafic rocks. Magnetite grains coexist with serpentine and magnesite (Fig. 7a–c). It is likely that some magnetite crystallized during serpentinization, while other magnetite crystallized during carbonation of serpentinite (Stage A in Fig. 11). Since sulphides fill interstitial gaps between magnetite (Fig. 8b–d), they postdated magnetite. Coexistence of sulphides and (high-Fe) magnesite in carbonated serpentinite (Fig. 7a–c), talc–carbonate rocks (Fig. 8e–f, Fig. 9a–c, g), and listwaenite (Fig. 10a, d–f) suggests that sulphides precipitated from fluid during carbonation of serpentinite (Stage B in Fig. 11).

6. Mineral chemistry

Serpentine in carbonated serpentinite is variable in composition (Table 3). It contains 0.07–0.34 wt% NiO and 0.04–0.37 wt% Cr_2O_3. Representative compositions of magnetite are listed in Table 4. Magnetite in carbonated serpentinite contains 0.22–0.47 wt% NiO and < 2.63 wt% Cr_2O_3. Magnetite in talc–carbonate rocks contains lower NiO (0.11–0.21 wt%) and similar Cr_2O_3 (0.22–2.95 wt%) compared with magnetite in carbonated serpentinite. Magnetite in listwaenite contains relatively lower NiO (< 0.11 wt%) and Cr_2O_3 (< 0.13 wt%) (Fig. 12).

Pyrite, violarite, millerite, pyrrhotite, pentlandite, and Fe-bearing siegenite are Ni-bearing sulphides in the Jianchaling nickel deposit (Table 5). Compositions of the Ni-bearing sulphides are plotted in the Fe–Ni–S ternary diagram (Fig. 13a). No compositional zoning exists in an individual sulphide grain. Fe-bearing siegenite and pentlandite are enriched in Co (Fig. 13b). Millerite, violarite, pentlandite, and Fe-bearing siegenite contains Te (Fig. 13c).

Pyrrhotite, Fe-bearing siegenite, and pentlandite in sulphide–dolomite veins are variable in composition. The chemical formula of pyrrhotite is $Fe_{0.86–0.90}S$. It contains 0.51–0.67 wt% Ni and up to 0.15 wt% Co. The composition of Fe-bearing siegenite ($Co_{1.17–1.22}Ni_{1.23–1.28}Fe_{0.65–0.59}S_4$) is relatively Fe-rich and S-deficient compared with the empirical formula of siegenite, $(Ni, Co)_3S_4$. Fe-bearing siegenite contains 0.20–0.23 wt% Te. The chemical formula of pentlandite ($Fe_{3.81–4.02}Ni_{4.78–4.62}Co_{0.61–0.47}S_8$) is Co-rich and S-rich compared with the empirical formula of pentlandite ($(Fe, Ni)_9S_8$). The Fe/Ni atomic ratio of pentlandite varies from 0.81 to 0.85. Pentlandite contains 0.31–0.38 wt% Te.

Pyrite, violarite, and millerite in PMVC assemblage are Ni-bearing sulphides in talc–carbonate rocks and listwaenite. Sulphides in talc–-carbonate rocks have similar components to sulphides in listwaenite. The chemical formula of pyrite is $Fe_{0.99–1.02}S_2$. Pyrite contains 0.13–1.42 wt% Ni and up to 0.67 wt% Co. The composition of violarite ($Fe_{0.73–0.79}Ni_{2.23–2.20}S_4$) is slightly S-rich and Ni-rich compared with the ideal formula, $FeNi_2S_4$. Violarite contains 0.35–0.41 wt% Te. Millerite with formula of $Ni_{0.98–1.05}S$ contains 0.18–2.26 wt% Fe and 0.52–0.70 wt% Te.

7. Geochemistry

The geochemical characteristics of serpentinite (HJ48a and HJ48b), carbonated serpentinite (HJ44, HJ45, and HJ47), talc–carbonate rocks (HJ88, HJ89, HJ90a, HJ92, HJ93a, and HJ97, including low-grade ores), and listwaenite (HJ90b, HJ91, and HJ93b, Table 6) are compared in order to evaluate behaviours of elements during metasomatism in ultramafic rocks. Compared with primitive mantle, serpentinite is depleted in Cr, Co, Ni, and Cu, while carbonated serpentinite is depleted in Sc and Ti (Fig. 14a). Compared with primitive mantle, talc–carbonate rocks are enriched in Co, Ni, and Cu, and are depleted in Sc and Ti. The variations of transition element contents in talc–carbonate rocks are small. The variations of transition element contents (especially Co, Ni, and Cu) in listwaenite are large, which might be related to the local deformation of listwaenite (Qiu and Zhu, 2015). Serpentinite and carbonated ultramafic rocks in the Jianchaling nickel deposit share a

Table 2
Representative compositions of Cr-spinel, chromite, and Cr-bearing magnetite in talc–carbonate rocks by EPMA (in wt%, O = 4).

Mineral	Cr-spinel							Chromite						Cr-bearing magnetite						
SiO_2	bdl	bdl	bdl	bdl	bdl	bdl	bdl	bdl	0.08	0.09	bdl	bdl	bdl	bdl	bdl	bdl	bdl	bdl	bdl	bdl
TiO_2	0.10	bdl	bdl	bdl	bdl	bdl	bdl	bdl	bdl	bdl	bdl	bdl	bdl	bdl	bdl	bdl	bdl	bdl	bdl	bdl
Al_2O_3	17.65	16.49	16.98	16.90	17.69	17.85	16.93	17.00	16.25	3.31	0.30	0.43	0.39	0.57	bdl	0.06	bdl	bdl	bdl	bdl
Cr_2O_3	51.46	49.10	48.43	48.34	51.75	51.91	50.23	50.37	48.95	36.76	18.01	25.16	24.00	21.40	3.74	3.83	6.96	2.28	0.21	
FeO^T	19.13	26.37	28.48	26.47	17.69	17.80	22.75	24.22	31.38	59.51	74.60	67.61	69.95	71.92	90.07	90.17	86.83	90.17	93.44	
MnO	0.65	0.39	0.36	0.64	0.84	0.83	0.73	0.53	0.37	0.32	0.21	0.34	0.27	0.31	bdl	bdl	0.12	0.08	bdl	
NiO	0.09	bdl	bdl	bdl	bdl	bdl	bdl	bdl	0.07	0.23	0.20	0.25	0.32	0.22	0.47	0.28	0.24	0.50	0.46	
MgO	9.66	3.19	3.46	4.70	10.33	10.52	7.25	5.33	1.15	0.09	0.04	0.04	0.04	bdl	bdl	bdl	bdl	0.04	0.04	
CaO	bdl	bdl	bdl	bdl	bdl	bdl	bdl	bdl	bdl	bdl	bdl	bdl	bdl	bdl	bdl	bdl	bdl	bdl	bdl	
Total	98.82	95.63	97.75	97.12	98.39	98.92	98.01	97.53	98.18	100.28	93.50	93.92	94.99	94.46	94.32	94.35	94.22	93.17	94.24	
Si	0	0	0	0	0	0	0	0	0	0	0.003	0.003	0	0	0	0	0	0	0	
Ti	0.002	0	0	0	0	0	0	0	0	0	0	0	0	0	0	0	0	0	0	
Al	0.673	0.682	0.685	0.680	0.674	0.676	0.663	0.679	0.667	0.140	0.014	0.020	0.018	0.026	0	0.003	0	0	0	
Cr	1.317	1.363	1.311	1.304	1.323	1.319	1.320	1.349	1.347	1.046	0.551	0.769	0.725	0.649	0.113	0.115	0.210	0.069	0.006	
Fe^{3+}	0.006	0	0.001	0.015	0.002	0.005	0.013	0	0	0.811	1.430	1.204	1.257	1.323	1.887	1.882	1.791	1.931	1.989	
Fe^{2+}	0.512	0.824	0.814	0.741	0.476	0.473	0.620	0.716	0.927	0.980	0.983	0.982	0.978	0.984	0.983	0.990	0.984	0.974	0.985	
Mn	0.018	0.012	0.010	0.019	0.023	0.023	0.021	0.015	0.011	0.010	0.007	0.011	0.009	0.010	0	0	0.004	0.003	0	
Ni	0.002	0	0	0	0	0	0	0	0.002	0.007	0.006	0.008	0.010	0.007	0.014	0.009	0.007	0.015	0.014	
Mg	0.466	0.167	0.177	0.239	0.498	0.504	0.359	0.269	0.060	0.005	0.002	0.002	0.002	0	0	0	0	0.002	0.002	
Ca	0	0	0	0	0	0	0	0	0	0	0	0	0	0	0	0	0	0	0	
Sum	3.000	3.000	3.000	3.000	3.000	3.000	3.000	3.000	3.000	3.000	3.000	3.000	3.000	3.000	3.000	3.000	3.000	3.000	3.000	
$Cr/(Cr + Al + Fe^{3+})$	0.660	0.666	0.656	0.653	0.662	0.659	0.661	0.665	0.669	0.524	0.276	0.386	0.363	0.325	0.056	0.058	0.105	0.035	0.003	
$Al/(Cr + Al + Fe^{3+})$	0.337	0.334	0.343	0.340	0.337	0.338	0.332	0.335	0.331	0.070	0.007	0.010	0.009	0.013	0	0.001	0	0	0.001	
$Fe^{3+}/(Cr + Al + Fe^{3+})$	0.003	0	0.001	0.007	0.001	0.003	0.006	0	0	0.406	0.717	0.604	0.629	0.662	0	0.941	0.895	0.965	0.996	
$Mg/(Mg + Fe^{2+})$	0.477	0.168	0.178	0.244	0.511	0.516	0.367	0.273	0.060	0.005	0.002	0.002	0.002	0	0.001	0	0	0.002	0.002	

bdl = below detection limit.

similar moderate light REE-enrichment and nearly flat heavy REE patterns (Fig. 14b). The $(La/Yb)_N$ values for serpentinite, carbonated serpentinite, talc–carbonate rocks, and listwaenite samples are 6.24–6.46, 7.40–34.4, 5.29–41.8, and 2.56–28.6, respectively. Most samples show weak negative Ce anomalies ($\delta Ce = Ce_N/(La_N \times Pr_N)^{0.5}$ = 0.65–0.98) and negative Eu anomalies ($\delta Eu = Eu_N/(Sm_N \times Gd_N)^{0.5}$ = 0.28–0.72, except HJ45). These samples are all enriched in Th, U, and Pb, and most samples are depleted in Zr and Ti in the primitive mantle normalized trace element spider diagram (Fig. 14c).

The isocon diagram (Grant, 1986) has been widely applied for studying element fluxes in metasomatic systems. This method has been proven useful in studying Ni migration in carbonated ultramafic rocks (Le Vaillant et al., 2016). Heavy REE concentrations in serpentinite, carbonated serpentinite, and talc–carbonate rocks are close to the primitive mantle values (Fig. 14c). It is reasonable to assume that heavy REE was immobile in the metasomatic system as no mineral enriched in heavy REE occurs in serpentinite and carbonated ultramafic rocks.

In the serpentinite versus carbonated serpentinite isocon diagram (Fig. 15a), the isocon defined by linear regression of heavy REE overlaps the constant mass line, suggesting that there was little mass change when serpentinite was transformed into carbonated serpentinite. Ni, Co, Cu, Mo, Mn, Sr, Ba, La, and Ce are enriched in carbonated serpentinite, while mass loss of Li, Rb, Cs, Zr, Nb, and Ti occurs.

In the carbonated serpentinite versus talc–carbonate rocks isocon diagram (Fig. 15b), the isocon is parallel to the constant mass line lying below it, suggesting that carbonation process caused mass increase in talc–carbonate rocks. Ni, Co, Cu, Li, and Pb are enriched in talc–carbonate rocks, while mass loss of Rb, Cs, Ba, Sr, and Zr occurs.

8. Discussions

8.1. Hydrothermal origin

There is an argument about whether the Jianchaling nickel deposit has a magmatic origin or a hydrothermal origin. Disseminated and massive high-grade ores with pyrrhotite–pentlandite assemblage show sideronitic texture (Wang et al., 2002). Exsolved pentlandite and magnetite in pyrrhotite suggest a monosulphide solid solution precursor (Zhang et al., 1986). These authors suggested a magmatic origin for high-grade ores. However, the facts that the ore bodies postdated albite porphyry, and sulphides postdated chromite and magnetite in talc–-carbonate rocks and listwaenite suggest a hydrothermal origin for the deposit (Jiang et al., 2010).

Our observations show that the PMVC assemblage in talc–carbonate rocks fill interstitial gaps between magnetite and replace magnetite (Fig. 8c–d). Carbonated serpentinite, talc–carbonate rocks, and listwaenite successively formed during carbonation of serpentinite. No sulphide occurs in serpentinite where content of carbonate minerals is below 5 vol%. Pyrite, millerite, and chalcopyrite coexist with magnesite in carbonated serpentinite (Fig. 7a–d). Pyrite, violarite, millerite, and chalcopyrite coexist with magnesite in talc–carbonate rocks (Fig. 9a–c). Violarite does not occur in carbonated serpentinite, while it occurs in talc–carbonate rocks and listwaenite. Talc–carbonate rocks and listwaenite contains more abundant pyrite and millerite (5–15 vol%) compared with carbonated serpentinite (< 5 vol%). Accompanied with carbonation of serpentinite, species and contents of Ni-bearing sulphides in carbonated ultramafic rocks increased. Magnesite in talc–-carbonate rocks and listwaenite crystallized at different stages. Since high-Fe magnesite postdated magnesite, coexistence of high-Fe magnesite and sulphides in talc–carbonate rocks and listwaenite (Figs. 8e–f, 10a) suggests that more abundant sulphides formed at a late stage in carbonation process. These observations support a hydrothermal origin for the low-grade ores with the PMVC assemblage. Hydrothermal activities must play a key role in forming the Jianchaling nickel deposit as low-grade ores with PMVC assemblage account for

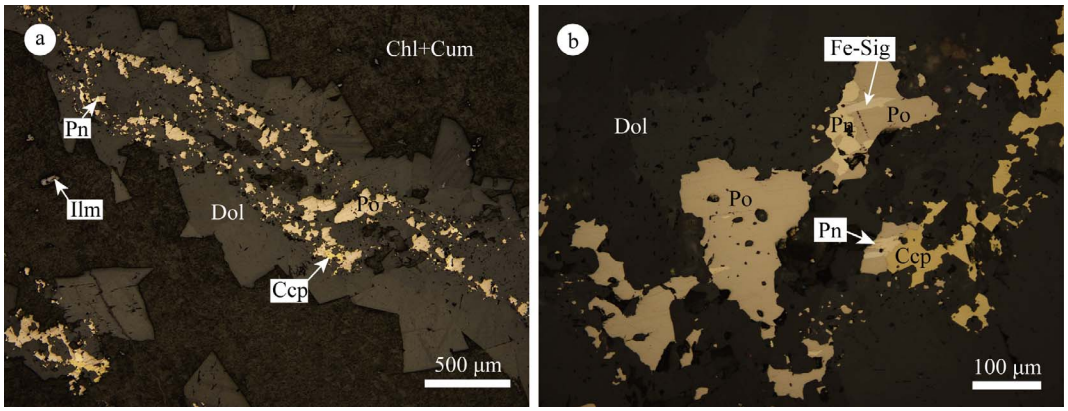

Fig. 6. Photomicrographs showing sulphide–dolomite veins in chlorite schist, reflected light. (a) A sulphide–dolomite vein crosscutting chlorite schist, reflected light. (b) Intergrowth of pentlandite, pyrrhotite, chalcopyrite, and Fe-bearing siegenite in a sulphide–dolomite vein, reflected light. Ccp – chalcopyrite, Chl – chlorite, Cum – cummingtonite, Dol – dolomite, Fe-Sig – Fe-bearing siegenite, Ilm – ilmenite, Pn – pentlandite, and Po – pyrrhotite.

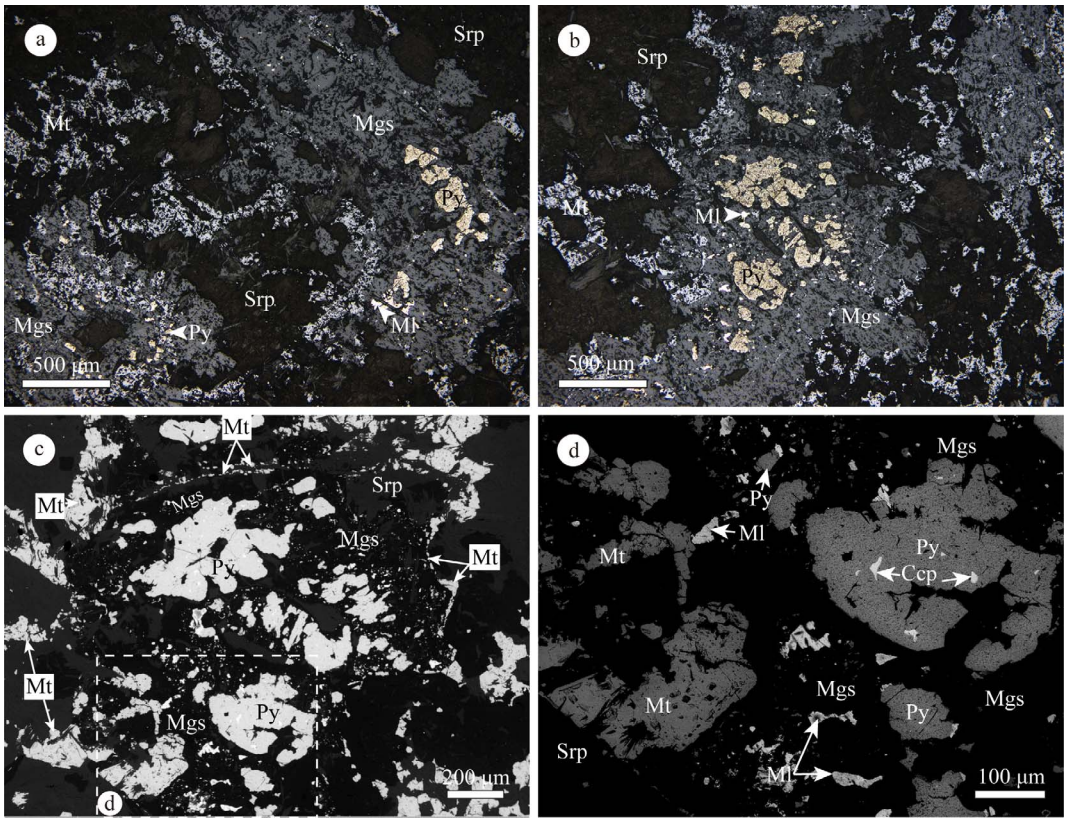

Fig. 7. Sulphides and magnetite in carbonated serpentinite. (a–c) Sulphides coexisting with magnesite and magnetite coexisting with serpentine or magnesite. (d) Chalcopyrite enclosed in pyrite and pyrite–millerite within magnesite matrix. a and b, reflected light, c and d, BSE. Ccp – chalcopyrite, Mgs – magnesite, Ml – millerite, Mt – magnetite, Py – pyrite, and Srp – serpentine.

70 wt% nickel resource in the deposit.

There are three possible sources of Ni: Ni-bearing silicate minerals in ultramafic rocks (Zaccarini and Garuti, 2008; González-Álvarez et al., 2013a; Loukola-Ruskeeniemi and Lahtinen, 2013), Ni-bearing oxides in ultramafic rocks (Ahmed et al., 2009), and sulphides in high-grade ores (Molnár et al., 1999; Keays and Jowitt, 2013). The NiO contents of magnetite from talc–carbonate rocks (0.11–0.21 wt%) and listwaenite (< 0.11 wt%) in the Jianchaling nickel deposit are obviously lower than that in their host rocks (carbonated serpentinite, 0.22–0.47 wt%, Fig. 12, Table 4). The NiO contents of magnetite decrease with progressive carbonation of serpentinite. This suggests that Ni in magnetite contributed to the formation of the PMVC assemblage. Serpentine with

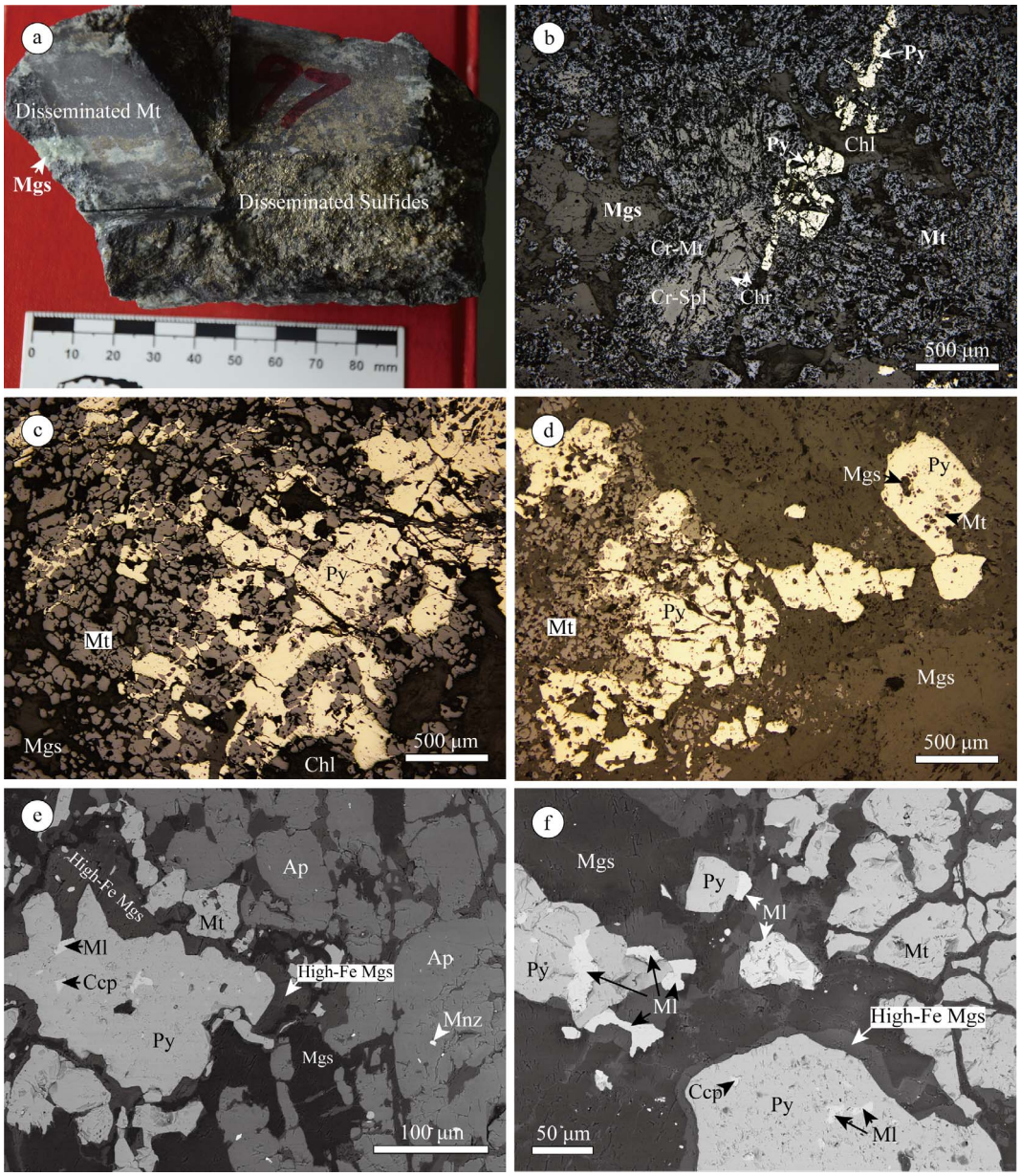

Fig. 8. Photograph (a) and photomicrographs (b–f) showing the relationships between magnetite, apatite, sulphides, and magnesite in talc–carbonate rocks. (b) Pyrite veins cutting through Cr-spinel–chromite–Cr-bearing magnetite assemblage. (c) Anhedral pyrite replacing magnetite. (d) Magnetite enclosed in subhedral pyrite. (e) Magnetite coexisting with apatite and monazite. (f) High-Fe magnesite crosscutting magnesite and surrounding sulphides. b–d, reflected light, e and f, BSE. Ap – apatite, Ccp – chalcopyrite, Chl – chlorite, Chr – chromite, Cr-Mt – Cr-bearing magnetite, Cr-Spl – Cr-spinel, Mgs – magnesite, Ml – millerite, Mnz – monazite, Mt – magnetite, and Py – pyrite.

NiO contents of 0.07–0.34 wt% (Table 3) is the dominant Ni-bearing silicate mineral in serpentinite. Progressive carbonation of serpentinite may have also liberated Ni and contributed to the ore forming processes. Thus, decomposition of magnetite and serpentinite during carbonation of serpentinite provided Ni to form the Jianchaling hydrothermal nickel deposit.

8.2. Constraints of the ore-forming environment

Thermal stability fields for Fe–Ni sulphides can be estimated based on S mole fraction and Ni mole fraction of sulphide assemblages (Vaughan and Craig, 1978; Waldner and Pelton, 2004; Waldner, 2009). Sulphur mole fraction of Fe–Ni sulphide assemblage (pyrite, millerite, violarite) in talc–carbonate rocks and listwaenite ranges from 0.50 (NiS, millerite) to 0.67 (pyrite, FeS_2) with an average value of 0.58, close to the S mole fraction of violarite (0.57). Violarite coexists with millerite in talc–carbonate rocks and listwaenite. When millerite accounts for a small portion (< 5 vol%) in intergrowth of violarite–millerite (Fig. 9b–c), Ni mole fraction is about 0.32. When millerite accounts for ~50 vol% in intergrowth of violarite–millerite (Fig. 9d and f), Ni mole fraction is about 0.41. Waldner (2009) constructed a Ni mole fraction – temperature phase diagram of the Fe–Ni–S system at a constant S mole

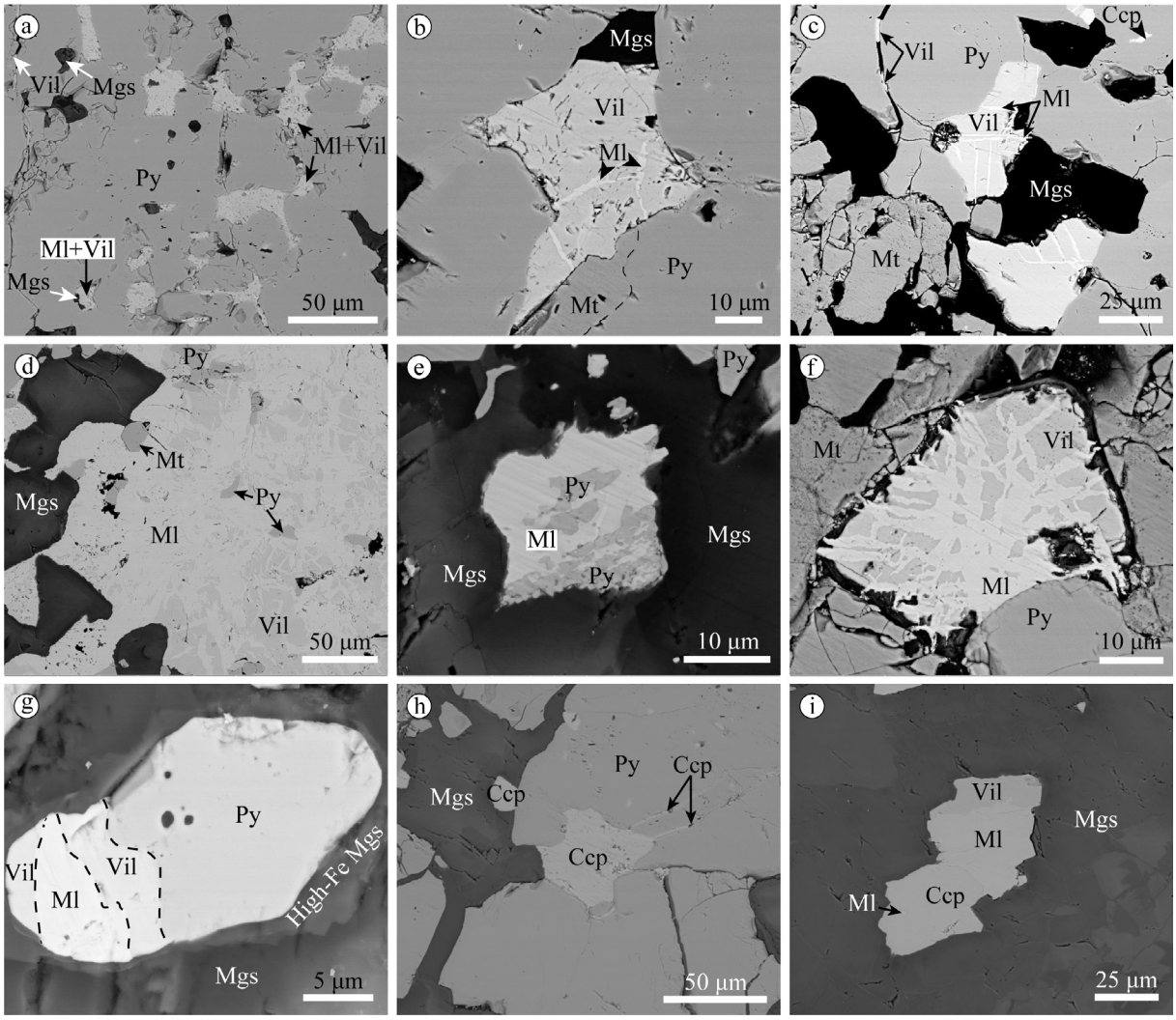

Fig. 9. BSE images of pyrite, violarite, millerite, and chalcopyrite in talc–carbonate rocks. (a–b) Irregular violarite–millerite–magnesite assemblage in the fractures of pyrite and interstitial gaps between pyrite. (c) Violarite and millerite replacing pyrite. (d) Relict pyrite enclosed in violarite and millerite. (e) Relict pyrite enclosed in millerite. (f) Intergrowth of millerite and violarite. (g) High-Fe magnesite crosscutting magnesite and surrounding pyrite–violarite–millerite assemblage. (h) Chalcopyrite veinlets crosscutting pyrite. (i) Chalcopyrite coexisting with violarite and millerite. Ccp – chalcopyrite, Mgs – magnesite, Ml – millerite, Mt – magnetite, Py – pyrite, and Vil – violarite.

fraction of 0.57 (Fig. 16). Because the S mole fraction for the phase diagram is close to that of Fe–Ni sulphide assemblage in talc–carbonate rocks and listwaenite, the phase diagram can be used to evaluate the ore-forming temperature in the Jianchaling nickel deposit. Thermal stability fields for intergrowths of violarite–millerite at Ni mole fraction of 0.32 and 0.50 are around 270 °C (543 K) and below 297 °C (570 K), respectively (shaded area in Fig. 16). Thus, the formation temperature of Fe–Ni sulphides in talc–carbonate rocks and listwaenite is slightly lower than 300 °C.

Silicate minerals and carbonate minerals buffer physicochemical conditions in fluids in serpentinite and carbonated ultramafic rocks (Eckstrand, 1975; Frost, 1985). Coexistence of sulphides and magnesite suggests that the talc–magnesite–quartz assemblage buffered fluid during ore-forming process in the deposit. From serpentinite to talc–carbonate rocks and listwaenite, transformation of serpentine into magnesite can be expressed by the following reactions (Kelemen et al., 2011; Ulrich et al., 2014):

$$2Mg_3Si_2O_5(OH)_{4\,serpentinite} + 3(2H^+ + CO_3^{2-}) = Mg_3Si_4O_{10}(OH)_{2\,talc} + 3MgCO_{3\,magnesite} + 6H_2O \quad (a)$$

$$Mg_3Si_2O_5(OH)_4 + 3(2H^+ + CO_3^{2-}) = 3MgCO_3 + 2SiO_{2\,quartz} + 5H_2O \quad (b)$$

The best efficiency for precipitation of magnesite is at pH 8–11, and the optimum occurs at pH 9 (Teir et al., 2007). Since sulphides coexist with magnesite, sulphides also crystallized at pH 8–11.

To constrain oxygen fugacity (fO_2) and sulphur fugacity (fS_2) during ore-forming process of PMVC assemblage in the Jianchaling nickel deposit, a log fO_2 – log fS_2 phase diagram is constructed to display the stability fields of Fe–Ni–Cu sulphides and iron oxides at 300 °C, 50 MPa (Fig. 17). The Gibbs free energies of formation of pyrrhotite ($Fe_{0.875}S$), pyrite (FeS_2), magnetite (Fe_3O_4), hematite (Fe_2O_3), heazlewoodite

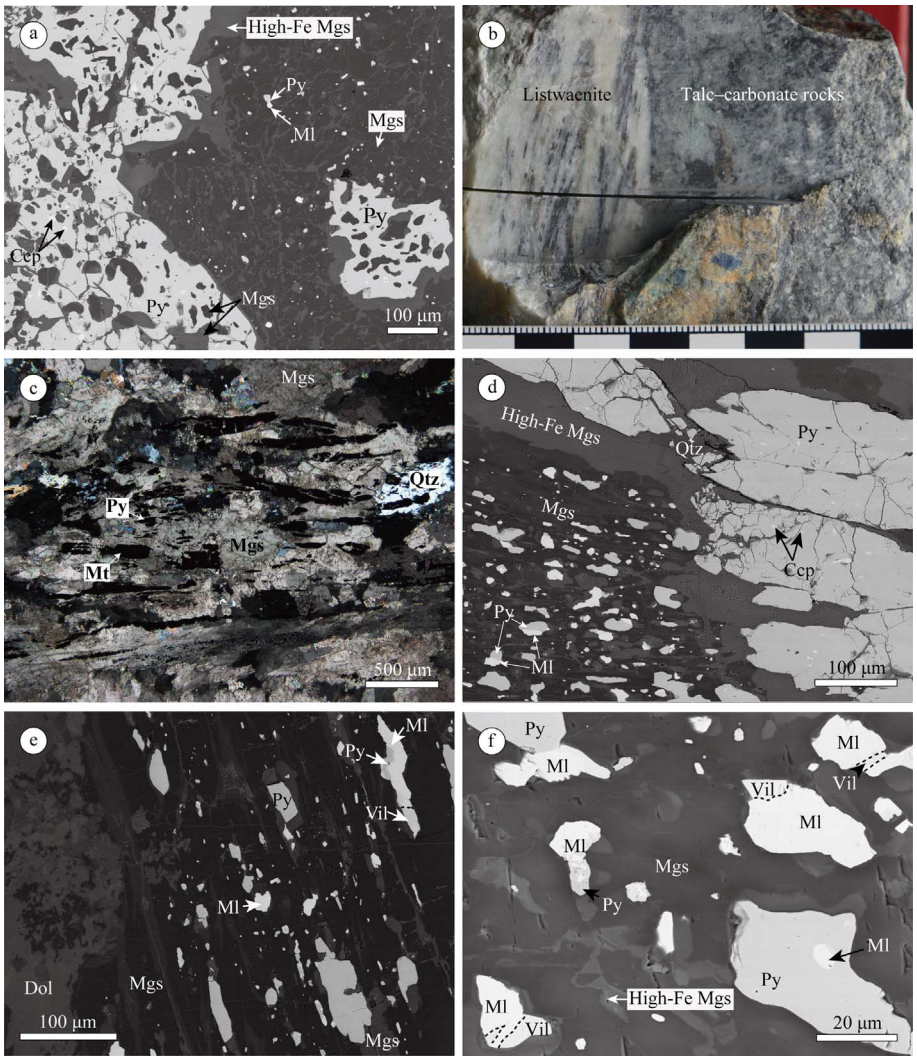

Fig. 10. (a) BSE image showing high-Fe magnesite coexisting with pyrite in listwaenite. (b) Photograph showing boundary between locally deformed listwaenite and talc–carbonate rocks. (c) A foliation fabric of locally deformed listwaenite. Magnesite, quartz, magnetite, and sulphides are distributed along the fabric, cross-polarized light. (d) BSE image showing high-Fe magnesite coexisting with pyrite in foliation fabrics. (e–f) BSE image showing coexistence of millerite, violarite, and pyrite in foliation fabrics. Ccp – chalcopyrite, Mgs – magnesite, Ml – millerite, Mt – magnetite, Py – pyrite, Qtz – quartz, and Vil – violarite.

(Ni_3S_2), millerite (NiS), polydymite (Ni_3S_4), vaesite (NiS_2), chalcopyrite ($CuFeS_2$), bornite (Cu_5FeS_4), and S_2 at 300 °C are from Simon and Essene (1996). Based on the three-sublattice modal (Waldner, 2009), the Gibbs free energy of formation of violarite ($Fe_{0.75}Ni_{2.25}S_4$) at 300 °C is −389.37 kJ/mol. The stability boundaries between Fe–Ni–Cu sulphides and iron oxides in the phase diagram are calculated using the Van't Hoff equation based on their thermodynamic properties. The CH_4–CO_2 buffer and the HS^-–SO_4^{2-} buffer at 300 °C, 50 MPa, pH 8 are calculated using the SUPCRT92 software with the slop98.dat database (Johnson et al., 1992). Involved reactions in the log fO_2 – log fS_2 phase diagram are listed in Table 7.

The fO_2 and fS_2 values for the ore-forming environment are estimated based on the following facts. (a) Stage A: Magnetite–magnesite assemblage formed in carbonated serpentinite. (b) Stage B: PMVC–magnesite assemblage formed in talc–carbonate rocks and listwaenite. Physicochemical conditions in fluid are supposed to correspond to the stability field shared by pyrite, millerite, violarite, and chalcopyrite. (c) Sufficient CO_2 was required in fluid to transform serpentine into magnesite. Therefore, fO_2 in fluid is supposed to be higher than the CH_4–CO_2 buffer. (d) Sufficient H_2S or HS^- was required in fluid to produce sulphides in carbonated ultramafic rocks. When pH ranges from 8 to 11 (the best efficiency for precipitation of magnesite), HS^- is the dominant form of sulphur in fluid (Heinrich and Candela, 2014). Therefore, fO_2 in fluid is supposed to be lower than the HS^-–SO_4^{2-} buffer. Because thermodynamic calculations suggest that the HS^- – SO_4^{2-} buffer at pH 8, 300 °C, 50 MPa (log fO_2 = −31.8) is lower than the magnetite–hematite buffer at 300 °C, 50 MPa (log fO_2 = −31.1), we only consider the situation where log fO_2 is lower than the HS^- – SO_4^{2-} buffer in Fig. 17.

Compared with magnetite–magnesite assemblage (Stage A), PMVC–magnesite assemblage crystallized from fluid with higher fS_2 (Stage B). PMVC assemblage in talc–carbonate rocks and listwaenite crystallized when log fO_2 values varied from −34.5 to −31.8 and log fS_2 values varied from −10.3 to −9.2 at 300 °C, 50 MPa (Fig. 17).

8.3. Mechanism of nickel precipitation

Millerite is the dominant Ni-bearing mineral in ores with PMVC assemblage in the Jianchaling nickel deposit. Millerite can form by fluid alteration of Ni-bearing sulphides such as pentlandite (Frost, 1985), or

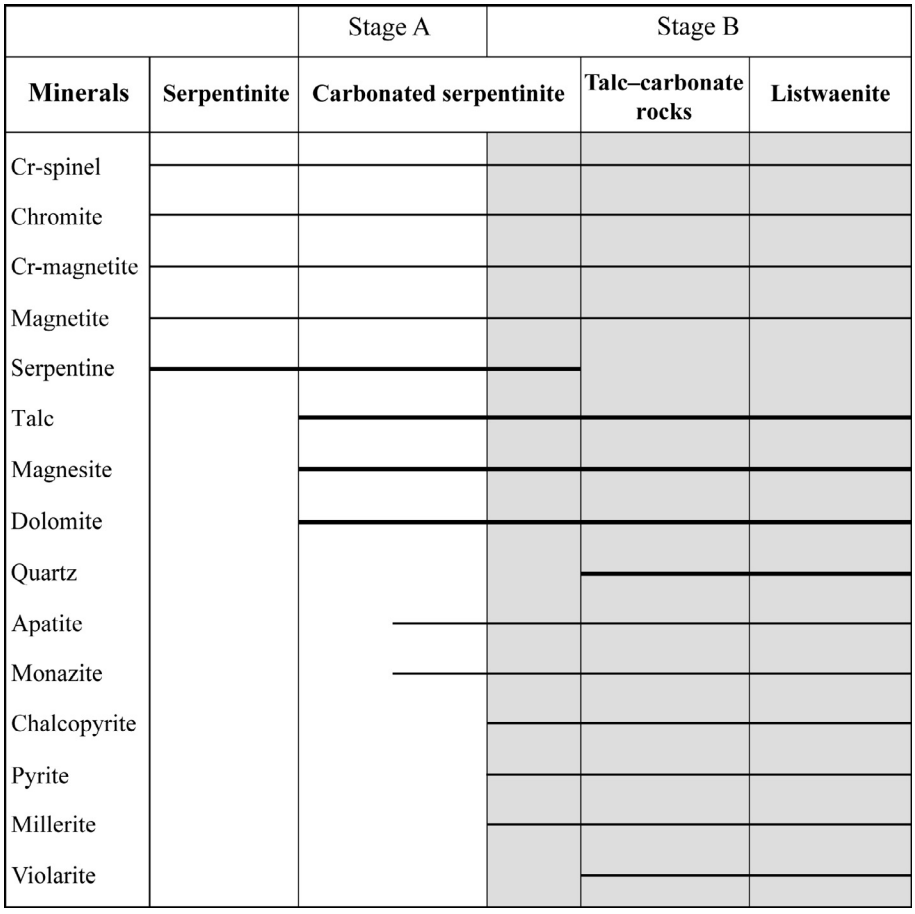

Fig. 11. Mineralogical variation within different serpentinite and carbonated ultramafic rocks present in the Jianchaling nickel deposit. Stage A: Serpentine–magnesite–magnetite. Stage B (shaded area): Magnesite–talc–quartz–sulphides.

Table 3
Representative compositions of serpentine in carbonated serpentinite by EPMA (in wt%).

	1	2	3	4	5	6
SiO_2	44.75	42.86	43.72	42.85	44.98	45.16
TiO_2	bdl	0.07	bdl	bdl	bdl	bdl
Al_2O_3	0.54	0.82	0.74	0.17	0.14	0.20
Cr_2O_3	0.05	0.04	0.05	0.27	0.16	0.37
FeO^T	2.98	6.85	5.39	5.35	3.33	4.49
MnO	bdl	0.05	0.11	bdl	bdl	0.04
NiO	0.12	0.21	0.19	0.07	0.07	0.34
MgO	39.39	37.79	37.81	39.43	39.25	38.16
CaO	0.03	bdl	bdl	bdl	bdl	0.05
Total	87.86	88.69	88.01	88.14	87.93	88.81

direct precipitation form fluid (Liu et al., 2012). Nickel contents of millerite are higher than those of other sulphides in PMVC assemblage (Fig. 13). Millerite commonly occurs in interstitial gaps between pyrite (Fig. 9a–c), and coexist with magnesite (Fig. 9e–g, Fig. 10e–f). These observations suggest that millerite directly precipitated from Ni and HS^--bearing fluid.

Previous studies suggest that chloride complexes are the dominant transporting agents of nickel (II) in fluid at 250–300 °C (Liu et al., 2012; Tian et al., 2012; Seward et al., 2014). Because the formation temperature of PMVC assemblage is slightly lower than 300 °C (Fig. 16), nickel chloride complexes are the dominant existing forms of nickel in fluid in the Jianchaling nickel deposit. Fluid in equilibrium with talc–carbonate rocks and listwaenite is at pH 8–11. As pyrite had formed before precipitation of nickel sulphides (Fig. 9a–e), nickel sulphides formed in reducing conditions. HS^- was the dominant existing form of sulphur in fluid. Based on these preconditions, the following reaction (Liu et al., 2012) can describe the precipitation mechanism of Ni-bearing sulphides in the Jianchaling nickel deposit:

$$NiCl_x^{2-x} + HS^- \rightleftharpoons NiS + H^+ + xCl^- \ (x=1, x=2, \text{or } x=3) \quad (c)$$

The precipitation–dissolution equilibrium of millerite is controlled by pH and HS^- activities in fluid based on reaction (c). Increasing pH and HS^- activities in fluid facilitate precipitation of millerite, whereas decreasing pH and HS^- activities in fluid facilitate dissolution of millerite.

Fluid pH increased during carbonation of serpentinite in the Jianchaling nickel deposit. Reactions (a) and (b), which transformed serpentine into magnesite during carbonation process, would have consumed H^+. H^+ concentration then decreased, facilitating precipitation of millerite.

The HS^- activities in fluid increased during carbonation of serpentinite. There is no sulphide present in serpentinite, while sulphides occur in carbonated serpentinite (Fig. 7). Compared with carbonated serpentinite, talc–carbonate rocks contain more abundant sulphides (Figs. 8, 9). Sulphides postdated magnetite, and formed in the late stages of carbonation process (Fig. 11). Thermodynamic analysis

Table 4
Representative compositions of magnetite from the Jianchaling nickel deposit by EPMA (in wt%, O = 4).

Rock	Carbonated serpentinite										
SiO_2	bdl	0.16	0.14	0.18	0.24	0.13	bdl	0.38	bdl	0.20	0.31
TiO_2	bdl	bdl	bdl	bdl	bdl	0.07	bdl	bdl	bdl	bdl	0.07
Al_2O_3	0.05	bdl	0.07	bdl	bdl	bdl	bdl	bdl	bdl	bdl	bdl
Cr_2O_3	2.03	0.15	0.15	0.13	bdl	0.15	0.28	0.78	0.44	0.10	0.25
Fe_2O_3	65.83	67.44	67.92	67.68	67.99	67.63	68.63	66.41	68.29	67.82	67.75
FeO	30.40	30.58	30.77	30.60	30.72	30.70	30.36	30.65	30.61	30.67	31.05
MnO	bdl	bdl	bdl	0.07	0.07	bdl	0.11	bdl	0.07	bdl	bdl
NiO	0.33	0.37	0.30	0.32	0.38	0.35	0.36	0.34	0.27	0.24	0.36
MgO	0.12	0.12	0.10	0.10	0.16	0.08	0.26	0.17	0.11	0.14	0.15
CaO	bdl	bdl	0.05	0.07	0.07	0.07	0.06	0.16	0.04	0.09	0.12
Total	98.76	98.83	99.56	99.22	99.69	99.26	100.12	99.05	99.87	99.36	100.18
Si	0	0.006	0.005	0.007	0.009	0.005	0	0.015	0	0.008	0.012
Ti	0	0	0	0	0	0.002	0	0	0	0	0.002
Al	0.002	0	0.003	0	0	0	0	0	0	0	0
Cr	0.063	0.005	0.005	0.004	0	0.005	0.009	0.024	0.013	0.003	0.008
Fe^{3+}	1.930	1.977	1.976	1.976	1.974	1.974	1.985	1.938	1.982	1.976	1.957
Fe^{2+}	0.990	0.996	0.995	0.993	0.991	0.996	0.976	0.994	0.987	0.993	0.997
Mn	0	0	0	0.002	0.002	0	0.004	0	0.002	0	0
Ni	0.010	0.012	0.009	0.010	0.012	0.011	0.011	0.011	0.008	0.007	0.011
Mg	0.007	0.007	0.006	0.006	0.009	0.005	0.015	0.010	0.006	0.008	0.009
Ca	0	0	0.002	0.003	0.003	0.003	0.002	0.007	0.002	0.004	0.005
Sum	3.003	3.003	3.001	3.001	3.001	3.001	3.001	2.998	3.001	2.999	2.999

Rock	Carbonated serpentinite							
SiO_2	0.63	0.11	0.35	0.12	0.19	0.12	0.56	0.07
TiO_2	bdl	bdl	bdl	0.08	bdl	bdl	bdl	bdl
Al_2O_3	bdl	bdl	bdl	bdl	bdl	bdl	0.05	bdl
Cr_2O_3	bdl	1.05	0.20	0.07	1.06	0.33	2.63	1.72
Fe_2O_3	66.84	66.85	67.28	67.79	66.98	67.44	63.97	66.07
FeO	30.81	30.70	30.58	30.84	30.96	30.63	30.83	30.60
MnO	bdl	bdl	0.08	bdl	bdl	bdl	bdl	0.11
NiO	0.42	0.29	0.33	0.22	0.30	0.34	0.47	0.35
MgO	0.25	0.04	0.21	0.07	0.07	0.09	0.26	bdl
CaO	0.25	0.05	0.13	bdl	bdl	bdl	0.08	bdl
Total	99.45	99.14	99.29	99.18	99.56	98.95	98.93	98.92
Si	0.024	0.004	0.014	0.005	0.007	0.005	0.022	0.003
Ti	0	0	0	0.002	0	0	0	0
Al	0	0	0	0	0	0	0.002	0
Cr	0	0.032	0.006	0.002	0.032	0.010	0.081	0.053
Fe^{3+}	1.940	1.954	1.959	1.980	1.948	1.975	1.865	1.936
Fe^{2+}	0.994	0.997	0.990	1.001	1.001	0.997	0.999	0.996
Mn	0	0	0.003	0	0	0	0	0.004
Ni	0.013	0.009	0.010	0.007	0.009	0.011	0.015	0.011
Mg	0.014	0.002	0.012	0.004	0.004	0.005	0.015	0
Ca	0.010	0.002	0.005	0	0	0	0.003	0
Sum	2.996	3.001	2.999	3.002	3.002	3.003	3.001	3.003

Rock	Talc–carbonate rocks							
SiO_2	0.11	bdl	bdl	0.37	0.09	0.19	2.94	2.15
TiO_2	bdl	bdl	bdl	bdl	bdl	bdl	bdl	bdl
Al_2O_3	bdl	bdl	bdl	0.15	bdl	bdl	0.04	1.03
Cr_2O_3	0.25	0.22	2.95	0.57	0.24	0.31	1.00	1.50
Fe_2O_3	67.84	68.69	66.89	67.25	68.07	67.62	59.81	62.33
FeO	30.90	31.01	31.49	31.40	30.88	30.71	34.44	31.16
MnO	bdl	bdl	bdl	bdl	bdl	bdl	bdl	bdl
NiO	0.11	0.21	0.15	0.14	0.11	0.16	0.11	0.19
MgO	bdl	bdl	bdl	0.03	0.04	0.14	bdl	1.94
CaO	bdl	bdl	bdl	0.05	bdl	0.05	bdl	bdl
Total	99.21	100.13	101.48	100.01	99.43	99.24	98.34	100.31
Si	0.004	0	0	0.014	0.003	0.007	0.114	0.080
Ti	0	0	0	0	0	0	0	0
Al	0	0	0	0.007	0	0	0.002	0.045
Cr	0.008	0.007	0.088	0.017	0.007	0.009	0.031	0.044
Fe^{3+}	1.982	1.990	1.909	1.944	1.984	1.972	1.739	1.748
Fe^{2+}	1.003	0.998	0.999	1.009	1.000	0.995	1.113	0.971
Mn	0	0	0	0	0	0	0	0
Ni	0.003	0.007	0.005	0.004	0.003	0.005	0.003	0.006
Mg	0	0	0	0.002	0.002	0.008	0	0.108
Ca	0	0	0	0.002	0	0.002	0	0
Sum	3.001	3.002	3.001	3.000	3.001	3.000	3.001	3.001

Rock	Listwaenite							
SiO_2	bdl	0.08	bdl	bdl	0.07	bdl	bdl	bdl
TiO_2	bdl	bdl	bdl	bdl	bdl	bdl	bdl	0.08
Al_2O_3	bdl	bdl	bdl	bdl	bdl	bdl	bdl	bdl
Cr_2O_3	0.11	bdl	bdl	0.07	0.13	0.13	bdl	bdl
Fe_2O_3	68.76	68.09	67.99	68.60	67.47	68.45	68.58	68.11
FeO	30.93	30.83	30.47	30.90	30.58	30.86	30.86	30.74

(*continued on next page*)

Table 4 (*continued*)

Rock	Listwaenite							
MnO	bdl	bdl	bdl	bdl	bdl	bdl	bdl	0.05
NiO	bdl	bdl	0.11	0.07	bdl	0.09	bdl	bdl
MgO	0.03	bdl	0.03	bdl	bdl	bdl	bdl	bdl
CaO	bdl	bdl	0.05	bdl	bdl	bdl	bdl	bdl
Total	99.83	99.00	98.70	99.63	98.25	99.53	99.44	98.97
Si	0	0.003	0	0	0.003	0	0	0
Ti	0	0	0	0	0	0	0	0.002
Al	0	0	0	0	0	0	0	0
Cr	0.003	0	0	0.002	0.004	0.004	0	0
Fe^{3+}	1.997	1.994	1.997	1.997	1.990	1.995	2.000	1.995
Fe^{2+}	0.998	1.003	0.995	0.999	1.003	0.999	1.000	1.001
Mn	0	0	0	0	0	0	0	0.002
Ni	0	0	0.003	0.002	0	0.003	0	0
Mg	0.002	0	0.002	0	0	0	0	0
Ca	0	0	0.002	0	0	0	0	0
Sum	3.000	3.000	2.999	3.001	3.000	3.001	3.000	3.000

bdl = below detection limit.

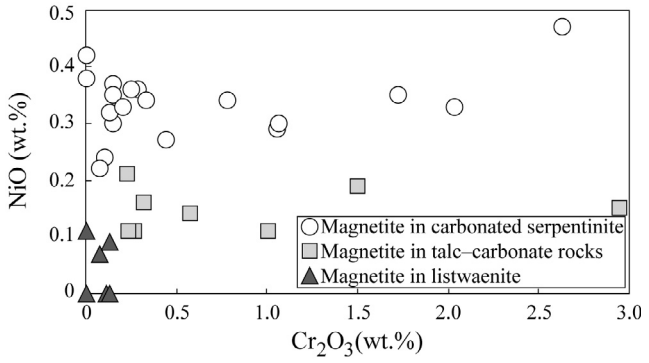

Fig. 12. Cr_2O_3 versus NiO variation diagram of magnetite in carbonated serpentinite, talc–carbonate rocks, and listwaenite.

suggests that PMVC–magnesite assemblage formed in an environment with higher fS_2 compared with magnetite–magnesite assemblage (Fig. 17). When HS^- is the dominant existing form of sulphur in fluid, fS_2 is mainly controlled by HS^- activities. Therefore, increasing fS_2 reflects increasing HS^- activities in fluid. Increasing HS^- activities in fluid during carbonation process also account for precipitation of millerite.

8.4. Genetic model

Previous studies on hydrothermal nickel deposits in ultramafic rocks focused on the relationships between alteration of host rocks and the associated Ni-bearing assemblages. For example, CO_2 and S-rich fluids progressively transformed serpentinite into talc–carbonate rocks, listwaenite, and pyrite–silicate rocks in the Eastern Metals deposit in Quebec (Auclair et al., 1993). Fluid from granodiorite dikes remobilized Ni from magmatic sulphides in ultramafic rocks. Pentlandite is the dominant Ni-bearing mineral in serpentinite and talc–carbonate rocks, whereas millerite and gersdorffite are the dominant Ni-bearing minerals in listwaenite and pyrite–silicate rocks. Gradients in redox conditions in the host rocks triggered the zonation of sulphide assemblages. The Avebury nickel deposit in Tasmania is the other typical hydrothermal Ni deposit hosted within an ultramafic suite (Keays and Jowitt, 2013). Accompanied with progressive alteration, more abundant Ni-bearing minerals are present in ultramafic rocks.

Similar to the Avebury nickel deposit and the Eastern Metals deposit, ore bodies in the Jianchaling nickel deposit are hosted in an ultramafic suite, which was intruded by granitoids (Fig. 2). Fig. 18 displays carbonation process in serpentinite and the accompanying ore-forming process of the Jianchaling hydrothermal nickel deposit. Granite porphyry and albite porphyry intruded into the ultramafic suite, dolomite, limestone, and sulphide-bearing slate (Fig. 18a), and caused metasomatism in these rocks. The emplacement of granite porphyry and albite porphyry activated Ni in serpentinized ultramafic rocks, and liberated CO_2 from dolomite and limestone. CO_2 entered serpentinite with fluid. Serpentine interacted with CO_2, and then magnesite and talc crystallized in carbonated serpentinite. When fluid pH increased, trace amounts of Fe–Ni sulphides precipitated from fluid (Fig. 18b). Talc–-carbonate rocks and listwaenite successively formed due to progressive reaction between CO_2-bearing fluid and carbonated serpentinite. The pH and HS^- activities in fluid increased during formation of talc–carbonate rocks and listwaenite. Increasing pH and HS^- activities in fluid facilitated precipitation of more abundant Ni-bearing sulphides, forming the PMVC assemblage in talc–carbonate rocks and listwaenite (Fig. 18c).

9. Conclusions

Hydrothermal activities in the Jianchaling ultramafic suite played a key role in the formation of the Jianchaling nickel deposit, in which Ni-bearing sulphides coexist with magnesite and postdate magnetite. Coexistence of sulphides and magnesite suggests that ore-forming conditions were controlled by carbonation of serpentinite. The $fO_2 - fS_2$ phase diagram shows that sulphides precipitated from fluid with log fO_2 values ranging from −34.5 to −31.8, and log fS_2 values ranging from −10.3 to −9.2. Increasing pH and HS^- activities could be responsible for precipitation of Ni-bearing sulphides in talc–carbonate rocks and listwaenite. CO_2-bearing fluid interacted with serpentinite and successively formed carbonated serpentinite, talc–carbonate rocks, and listwaenite. Triggered by carbonation, pH and HS^- activities increased, and Ni-bearing sulphides precipitated, finally forming the Jianchaling hydrothermal nickel deposit.

Table 5
Representative compositions of sulphides from the Jianchaling nickel deposit by EPMA (in wt%).

Mineral	Fe	As	S	Ni	Cu	Zn	Co	Se	Sb	Te	Total
Pyrite	46.36	0.12	52.98	0.59	bdl	bdl	0.09	bdl	bdl	bdl	100.14
Pyrite	46.66	bdl	53.29	0.17	bdl	bdl	0.04	bdl	bdl	bdl	100.19
Pyrite	45.66	0.12	52.90	0.27	bdl	bdl	0.64	bdl	bdl	0.02	99.64
Pyrite	46.21	0.09	53.27	0.23	bdl	bdl	0.67	bdl	bdl	bdl	100.49
Pyrite	46.32	bdl	53.04	0.35	bdl	bdl	0.09	0.03	bdl	0.02	99.84
Pyrite	46.13	bdl	52.94	0.45	bdl	bdl	0.05	bdl	bdl	bdl	99.60
Pyrite	45.60	bdl	52.53	1.25	bdl	bdl	0.05	bdl	bdl	bdl	99.46
Pyrite	45.65	bdl	52.31	1.42	bdl	bdl	0.04	bdl	bdl	bdl	99.43
Pyrite	45.34	bdl	52.34	1.27	bdl	bdl	0.05	bdl	0.02	bdl	99.01
Pyrite	46.09	bdl	52.80	0.62	bdl	bdl	0.08	bdl	bdl	bdl	99.58
Pyrite	46.29	0.07	52.54	0.42	bdl	bdl	0.28	bdl	bdl	bdl	99.63
Pyrite	46.81	0.03	52.61	0.13	bdl	bdl	0.31	0.04	bdl	bdl	99.95
Pyrite	46.82	0.06	52.22	0.15	bdl	bdl	0.04	bdl	bdl	bdl	99.34
Violarite	13.61	0.04	42.35	42.35	bdl	bdl	bdl	bdl	bdl	0.39	98.77
Violarite	13.79	bdl	42.51	42.92	bdl	bdl	0.03	0.08	bdl	0.35	99.71
Violarite	13.55	bdl	42.55	43.05	bdl	bdl	0.03	0.06	bdl	0.41	99.66
Violarite	14.71	bdl	42.49	42.43	bdl	bdl	0.17	0.04	bdl	0.38	100.22
Violarite	14.70	bdl	42.63	42.84	bdl	bdl	0.13	bdl	0.02	0.40	100.74
Millerite	0.89	bdl	35.39	63.41	bdl	bdl	bdl	bdl	bdl	0.57	100.26
Millerite	1.07	0.05	35.38	64.12	bdl	bdl	bdl	bdl	bdl	0.59	101.21
Millerite	0.82	bdl	35.42	63.31	bdl	bdl	bdl	0.03	bdl	0.67	100.25
Millerite	0.79	bdl	35.35	64.26	bdl	bdl	0.03	0.04	bdl	0.56	101.03
Millerite	1.99	0.06	35.10	62.79	bdl	bdl	0.03	bdl	0.03	0.58	100.59
Millerite	2.03	0.08	35.15	62.14	bdl	bdl	bdl	bdl	bdl	0.58	99.98
Millerite	2.26	0.04	34.89	61.96	bdl	bdl	0.03	0.06	bdl	0.52	99.76
Millerite	0.87	bdl	34.20	63.24	bdl	bdl	0.10	bdl	bdl	0.70	99.11
Millerite	0.23	0.05	34.11	64.61	bdl	bdl	0.05	0.14	bdl	0.70	99.90
Millerite	0.39	0.04	34.38	63.96	bdl	bdl	0.04	0.07	0.02	0.64	99.53
Millerite	0.18	bdl	34.57	64.52	bdl	bdl	0.08	bdl	bdl	0.67	100.01
Millerite	0.65	bdl	34.07	64.62	bdl	bdl	0.05	0.11	bdl	0.66	100.17
Millerite	2.25	bdl	34.31	62.52	bdl	bdl	0.08	bdl	bdl	0.59	99.79
Mineral	Fe	As	S	Ni	Cu	Zn	Co	Se	Sb	Te	Total
Pentlandite	27.91	0.04	32.54	34.29	bdl	bdl	3.89	bdl	bdl	0.36	99.02
Pentlandite	27.57	bdl	32.76	34.29	bdl	bdl	4.23	bdl	bdl	0.38	99.23
Pentlandite	27.51	bdl	32.78	34.73	bdl	bdl	4.00	bdl	bdl	0.36	99.39
Pentlandite	27.72	bdl	32.54	34.81	bdl	bdl	4.14	bdl	bdl	0.31	99.52
Pentlandite	27.69	0.04	32.93	34.64	bdl	bdl	4.64	bdl	bdl	0.31	100.25
Pentlandite	28.03	0.03	32.53	34.91	bdl	bdl	3.73	0.02	bdl	0.34	99.58
Pentlandite	27.55	0.06	33.05	35.18	bdl	bdl	3.61	0.04	bdl	0.38	99.87
Pentlandite	28.61	bdl	32.52	34.82	bdl	bdl	3.90	0.04	bdl	0.38	100.27
Pentlandite	27.49	bdl	32.54	35.22	bdl	bdl	3.56	0.02	bdl	0.34	99.17
Fe-Siegenite	11.83	0.09	41.60	23.22	bdl	bdl	22.34	bdl	bdl	0.23	99.31
Fe-Siegenite	10.88	0.03	41.86	23.55	bdl	bdl	23.27	bdl	bdl	0.20	99.80
Fe-Siegenite	10.97	bdl	41.28	23.93	bdl	bdl	23.16	bdl	bdl	0.20	99.54
Pyrrhotite	60.34	bdl	38.32	0.58	bdl	bdl	0.13	0.04	bdl	bdl	99.41
Pyrrhotite	59.34	0.08	39.33	0.58	bdl	bdl	0.10	bdl	bdl	bdl	99.45
Pyrrhotite	60.55	bdl	39.02	0.64	bdl	0.06	0.11	bdl	bdl	bdl	100.37
Pyrrhotite	59.73	bdl	39.54	0.51	bdl	bdl	0.09	bdl	bdl	bdl	99.88
Pyrrhotite	59.37	0.04	39.03	0.62	bdl	bdl	0.13	bdl	bdl	bdl	99.19
Pyrrhotite	60.25	bdl	39.50	0.64	bdl	bdl	0.13	bdl	0.02	bdl	100.56
Pyrrhotite	59.31	0.03	39.25	0.59	bdl	0.06	0.07	bdl	bdl	bdl	99.31
Pyrrhotite	59.24	bdl	39.18	0.58	bdl	bdl	0.09	bdl	0.02	bdl	99.12
Pyrrhotite	59.97	bdl	39.20	0.63	bdl	0.05	0.10	0.03	bdl	bdl	100.00
Pyrrhotite	59.31	bdl	39.32	0.67	bdl	bdl	0.13	0.04	bdl	bdl	99.48
Pyrrhotite	59.23	bdl	39.30	0.65	bdl	bdl	0.07	bdl	bdl	0.02	99.28
Pyrrhotite	59.31	bdl	39.26	0.65	bdl	bdl	0.15	bdl	bdl	bdl	99.36
Pyrrhotite	59.34	bdl	39.45	0.65	bdl	0.05	0.14	bdl	bdl	bdl	99.65
Pyrrhotite	59.63	0.03	39.08	0.62	bdl	bdl	0.07	0.05	bdl	bdl	99.48
Chalcopyrite	29.44	bdl	33.80	0.06	35.81	bdl	bdl	bdl	bdl	bdl	99.15
Chalcopyrite	29.72	bdl	33.92	0.03	35.16	0.06	0.08	0.09	bdl	bdl	99.04
Chalcopyrite	29.99	bdl	33.68	bdl	35.89	bdl	bdl	bdl	bdl	bdl	99.62
Chalcopyrite	29.36	bdl	34.37	bdl	35.49	bdl	0.05	bdl	0.02	bdl	99.30
Chalcopyrite	30.88	bdl	34.67	bdl	34.77	bdl	0.06	bdl	bdl	bdl	100.41
Chalcopyrite	30.42	bdl	33.73	bdl	34.74	0.10	0.03	0.04	bdl	bdl	99.10

bdl = below detection limit.

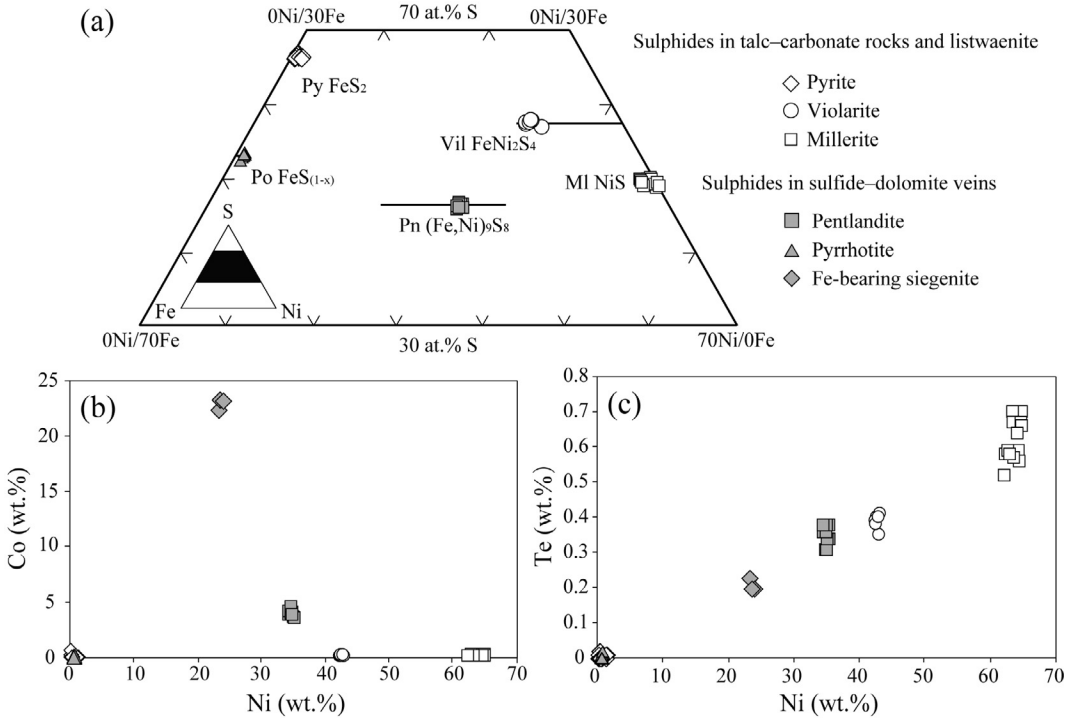

Fig. 13. Plots showing sulphide compositions in the Jianchaling nickel deposit based on EPMA data. (a) Sulphide compositions in the Fe–Ni–S ternary system. (b) Ni versus Co variation diagram. (c) Ni versus Te variation diagram.

Table 6
Representative compositions of trace elements in the Jianchaling deposit (by ICP-MS, ppm).

Sample	HJ48a	HJ48b	HJ44	HJ45	HJ47	HJ88	HJ89	HJ90	HJ92	HJ93	HJ97	HJ90b	HJ91	HJ93b
Li	12.8	13.3	3.75	2.15	1.67	4.25	3.65	2.95	2.10	3.47	7.43	0.76	1.77	1.91
Be	0.09	0.10	0.06	0.29	0.16	0.12	0.09	0.05	0.04	0.04	0.06	0.04	0.04	0.05
P	185	190	159	530	32.9	92.9	755	675	68.4	121	64.0	86.9	44.2	256
Sc	9.55	10.1	8.10	4.86	3.96	3.13	3.32	2.97	2.79	2.35	1.88	1.29	1.88	3.09
Ti	971	989	435	202	205	201	173	161	191	113	190	59.7	106	121
V	82.0	86.1	44.6	96.1	87.3	84.8	93.7	85.6	96.1	67.2	158	24.3	14.2	37.3
Cr	76.6	82.3	79.5	2260	1798	1537	1594	1141	986	1208	2214	332	280	703
Mn	710	740	2602	1514	1215	1610	1154	1075	1540	1657	1788	9285	7228	1548
Co	36.3	37.4	31.0	61.8	85.6	131	307	218	161	226	307	40.5	9.28	81.3
Ni	368	371	552	1367	2194	1970	2247	1923	1881	1986	2901	585	45.3	867
Ni*	380	354	571	1420	2007	1911	1958	1932	1775	1833	2500	626	31.2	889
Cu	5.31	4.83	11.3	30.3	61.7	166	275	125	128	185	265	72.1	6.39	64.8
Ga	6.95	7.26	5.83	3.24	3.22	4.71	4.97	5.28	4.87	3.91	4.72	1.37	1.32	3.08
Rb	13.8	14.4	8.27	1.08	0.50	0.93	0.29	0.27	0.41	0.46	0.67	1.86	3.04	5.55
Sr	21.8	12.1	101	13.7	25.0	11.9	11.8	25.3	14.0	11.3	21.9	16.2	18.2	14.3
Y	4.18	4.30	6.95	3.40	1.98	2.39	5.68	3.41	2.42	2.38	1.45	2.38	2.09	2.74
Zr	109	116	112	3.24	2.92	3.58	2.82	3.04	2.49	1.86	1.81	1.04	1.32	2.68
Nb	4.43	4.44	1.64	1.10	0.74	0.86	1.58	0.80	0.90	0.51	0.77	0.65	0.17	1.20
Mo	0.47	0.33	5.98	0.64	0.42	0.54	0.63	0.71	0.59	1.04	1.09	1.67	1.13	0.67
Sn	4.43	4.53	4.16	4.21	3.33	2.87	2.34	2.19	2.90	2.42	2.37	2.37	1.56	2.51
Cs	0.72	0.77	0.67	0.25	0.08	0.05	0.05	0.04	0.05	0.04	0.05	0.07	0.07	0.10
Ba	9.55	10.8	112	5.44	5.89	6.37	9.91	5.17	4.17	4.80	7.97	9.87	16.3	31.5
La	4.32	4.56	8.70	14.7	2.07	3.90	19.0	17.2	2.02	5.93	3.80	10.5	1.09	3.71
Ce	7.49	7.62	12.7	22.9	3.67	7.01	31.7	26.2	4.06	10.2	6.00	15.5	1.91	7.26
Pr	1.01	1.01	1.52	2.38	0.67	0.95	3.23	2.55	0.71	1.24	0.83	1.66	0.47	1.03
Nd	3.50	3.45	5.40	7.53	2.42	3.21	10.3	7.80	2.57	4.15	2.81	5.32	1.73	3.70
Sm	0.45	0.44	0.87	0.83	0.30	0.36	1.19	0.77	0.30	0.42	0.25	0.52	0.17	0.47
Eu	0.09	0.09	0.18	0.17	0.12	0.04	0.13	0.10	0.03	0.04	0.03	0.10	0.04	0.10
Gd	0.53	0.53	0.97	0.87	0.33	0.41	1.26	0.86	0.35	0.46	0.29	0.55	0.22	0.51
Tb	0.08	0.08	0.14	0.10	0.05	0.06	0.15	0.09	0.05	0.06	0.03	0.06	0.04	0.07
Dy	0.56	0.57	0.91	0.56	0.31	0.36	0.79	0.50	0.34	0.35	0.23	0.34	0.28	0.42
Ho	0.13	0.13	0.21	0.11	0.06	0.07	0.16	0.10	0.07	0.07	0.04	0.06	0.06	0.08
Er	0.42	0.43	0.66	0.30	0.17	0.21	0.46	0.28	0.22	0.22	0.14	0.19	0.20	0.25
Tm	0.07	0.07	0.10	0.05	0.03	0.03	0.07	0.04	0.04	0.04	0.02	0.03	0.04	0.04
Yb	0.47	0.48	0.69	0.29	0.19	0.25	0.41	0.28	0.26	0.28	0.17	0.25	0.29	0.29
Lu	0.08	0.09	0.12	0.05	0.03	0.04	0.06	0.05	0.04	0.05	0.03	0.04	0.05	0.05
Pb	2.18	3.14	4.76	2.04	4.01	4.10	4.59	5.47	7.09	4.48	8.45	4.49	3.40	9.22
Th	3.82	3.75	2.62	4.79	0.39	0.51	3.11	4.33	0.61	1.09	0.43	0.24	0.10	2.33
U	1.29	1.29	1.24	1.87	0.57	0.33	0.73	0.97	0.28	0.40	0.38	0.17	0.08	1.28
ΣREE	19.2	19.6	33.2	50.8	10.4	16.9	68.9	56.9	11.1	23.6	14.7	35.1	6.59	18.0
$(La/Yb)_N$	6.24	6.46	8.56	34.4	7.40	10.6	31.4	41.8	5.29	14.4	15.1	28.6	2.56	8.69
δCe	0.87	0.86	0.85	0.75	0.92	0.88	0.98	0.96	0.82	0.91	0.82	0.90	0.65	0.90
δEu	0.56	0.57	0.60	1.16	0.72	0.32	0.32	0.38	0.28	0.28	0.34	0.57	0.63	0.62

*Reanalysis of Ni using atomic absorption spectroscopy.
$\delta Eu = Eu/(Sm \times Gd)^{0.5}$.
$\delta Ce = Ce/(La \times Pr)^{0.5}$.

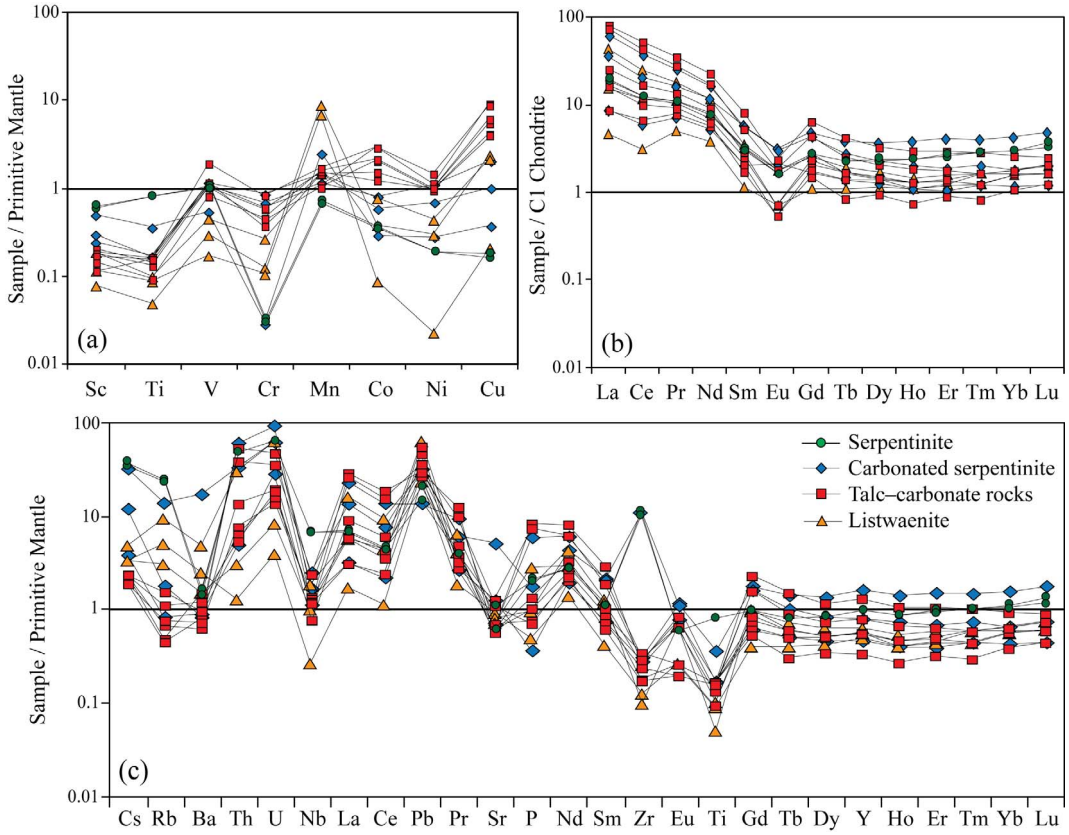

Fig. 14. (a) First-row transition element characteristics of samples from the Jianchaling nickel deposit, normalized to primitive mantle. (b) REE characteristics of ultramafic rocks, normalized to C1 chondrite. (c) Spidergram normalized to primitive mantle showing the representative trace element characteristics of ultramafic rocks. Reference data from McDonough and Sun (1995).

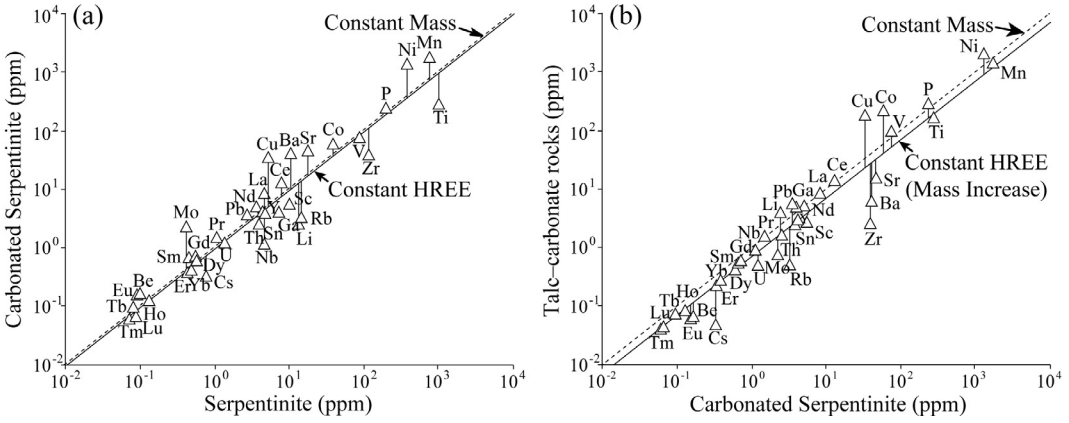

Fig. 15. (a) The logarithmic isocon diagram of trace elements in serpentinite versus carbonated serpentinite. (b) The logarithmic isocon diagram of trace elements in carbonated serpentinite versus talc–carbonate rocks, modified from Grant (1986).

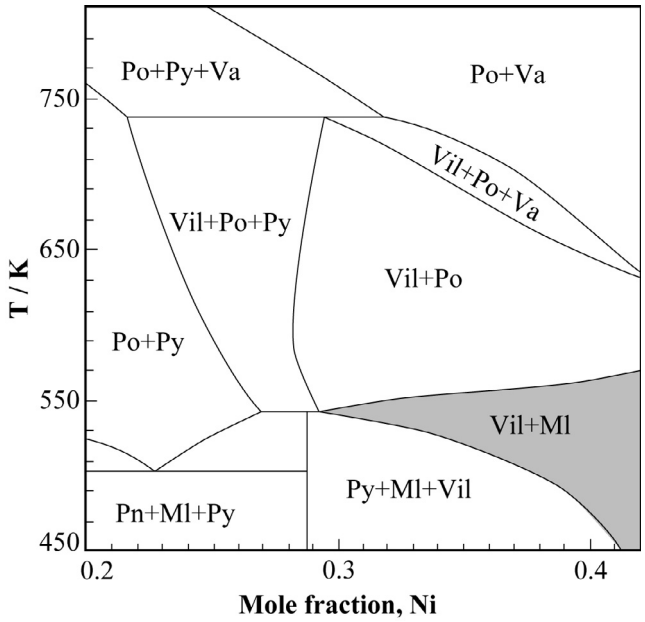

Fig. 16. Estimated stable temperature of Fe–Ni sulphides based on Ni mole fraction of sulphide assemblage at a constant S mole fraction of 0.571 (modified after Waldner, 2009). The shaded area represents the stability fields of millerite–violarite intergrowth in talc–carbonate rocks and listwaenite. Ml – millerite, Pn – pentlandite, Po – pyrrhotite, Py – pyrite, Vil – violarite, and Va – vaesite.

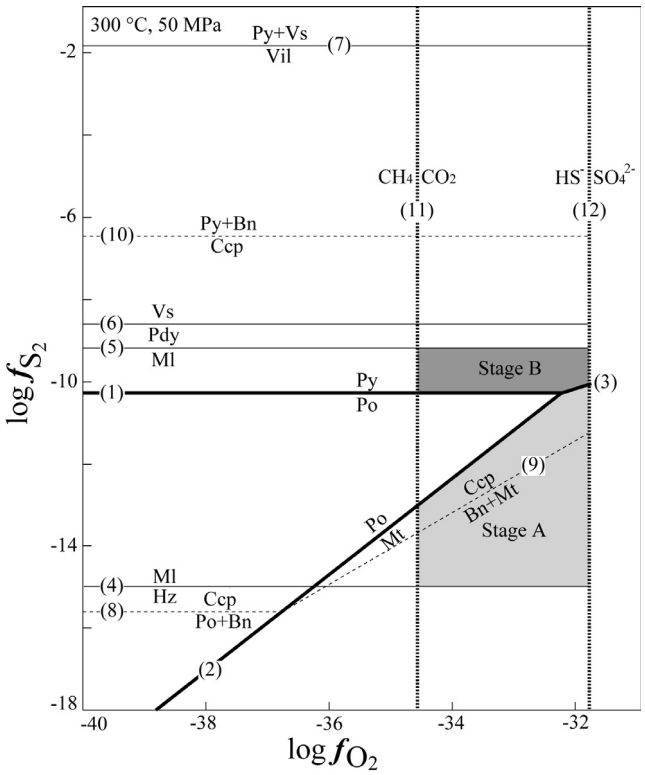

Fig. 17. Oxygen fugacity (fO_2) versus sulphur fugacity (fS_2) phase diagram constraining ore-forming conditions in the Jianchaling nickel deposit. Bold solid lines show stability boundaries between iron sulphides and iron oxides. Thin solid lines represent stability boundaries between nickel sulphides. Thin dotted lines show stability field of chalcopyrite. The bold dotted line between of CH_4 and CO_2 means the two components have equal concentration at this boundary (CH_4–CO_2 buffer). The bold dotted line between of HS^- and SO_4^{2-} means the two components have equal concentration at this boundary (HS^-–SO_4^{2-} buffer). Reactions controlling these boundaries are listed in Table 7. Stage A: magnetite–magnesite assemblage, Stage B: PMVC–magnesite assemblage. Bn – bornite, Ccp – chalcopyrite, Hz – heazlewoodite, Ml – millerite, Mt – magnetite, Pdy – polydymite, Po – pyrrhotite, Py – pyrite, Vil – violarite, and Vs – vaesite.

Table 7
Equilibria controlling the stability fields of the ore-forming system.

Reactions	Number
$8Fe_{0.875}S + 3S_2 = 7FeS_2$	(1)
$24Fe_{0.875}S + 14O_2 = 7Fe_3O_4 + 12S_2$	(2)
$3FeS_2 + 2O_2 = Fe_3O_4 + 3S_2$	(3)
$2Ni_3S_2 + S_2 = 6NiS$	(4)
$6NiS + S_2 = 2Ni_3S_4$	(5)
$Ni_3S_4 + S_2 = 3NiS_2$	(6)
$4Ni_{2.25}Fe_{0.75}S_4 + 4S_2 = 3FeS_2 + 9NiS_2$	(7)
$7Cu_5FeS_4 + 32Fe_{0.875}S + 5S_2 = 35CuFeS_2$	(8)
$15CuFeS_2 + 8O_2 = 3Cu_5FeS_4 + 4Fe_3O_4 + 9S_2$	(9)
$5CuFeS_2 + S_2 = Cu_5FeS_4 + 4FeS_2$	(10)
$CH_4 + 2O_2 = CO_2 + 2H_2O$	(11)
$HS^- + 2O_2 = SO_4^{2-} + H^+$	(12)

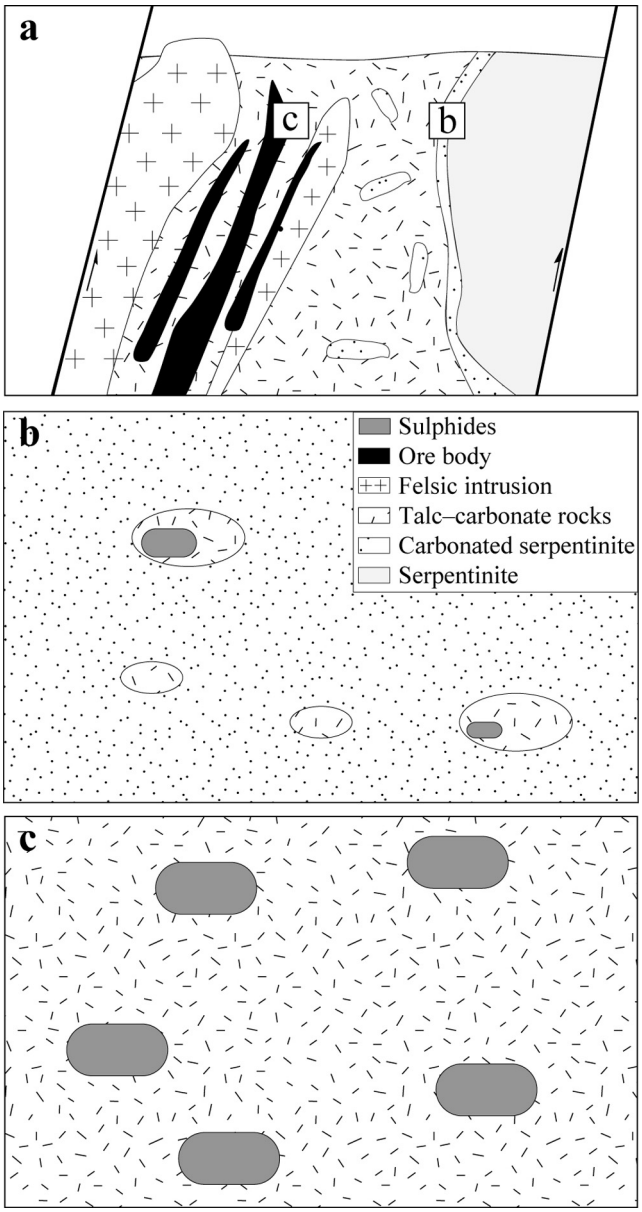

Fig. 18. The genetic model showing ore-forming process in the Jianchaling nickel deposit. (a) Alteration zoning controls the distribution of ore bodies. (b) Trace amounts of sulphides and magnesite precipitated in carbonated serpentinite. (c) More sulphides and magnesite precipitated in talc–carbonate rocks, forming ores with PMVC assemblage.

Acknowledgments

Critical comments and suggestions by anonymous reviewers helped us to improve this paper significantly. Guiming Shu and Xiaoli Li provided assistance with EPMA. Fang Ma and Libing Gu provided assistance during ICP-MS analysis. This study is financially supported by the Natural Science Foundation of China (Grant No. 41672047, 41372062).

Conflict of interest

There is no possible conflict of interest related to this manuscript.

References

Ahmed, A.H., Arai, S., Ikenne, M., 2009. Mineralogy and paragenesis of the Co–Ni arsenide ores of Bou Azzer, Anti-Atlas, Morocco. Econ. Geol. 104, 249–266.
Auclair, M., Gauthier, M., Trottier, J., Jebrak, M., Chartrand, F., 1993. Mineralogy, geochemistry, and paragenesis of the Eastern Metals serpentinite-associated Ni–Cu–Zn deposit, Quebec Appalachians. Econ. Geol. 88, 123–138.
Barnes, S.J., Wells, M.A., Verrall, M.R., 2009. Effects of magmatic processes, serpentinization, and talc–carbonate alteration on sulfide mineralogy and ore textures in the Black Swan disseminated nickel sulfide deposit, Yilgarn Craton. Econ. Geol. 104, 539–562.
Barnes, S.J., Cruden, A.R., Arndt, N., Saumur, B.M., 2016. The mineral system approach applied to magmatic Ni–Cu–PGE sulphide deposits. Ore Geol. Rev. 76, 296–316.
Dai, J.Z., Chen, L.X., Shi, X.F., Wang, R.T., Li, F.R., Zheng, C.Y., 2014. Geochronology of acid intrusive rocks of the Jianchaling nickel deposit in Lueyang, Shaanxi and its metallogenic implications. Acta Geol. Sinica 88, 1861–1873 (in Chinese with English abstract).
Eckstrand, O.R., 1975. The Dumont serpentinite; a model for control of nickeliferous opaque mineral assemblages by alteration reactions in ultramafic rocks. Econ. Geol. 70, 183–201.
Frost, B.R., 1985. On the stability of sulfides, oxides, and native metals in serpentinite. J. Petrol. 26, 31–63.
González-Álvarez, I., Sweetapple, M., Lindley, I.D., Kirakar, J., 2013a. Hydrothermal Ni: Doriri Creek, Papua New Guinea. Ore Geol. Rev. 52, 37–57.
González-Álvarez, I., Pirajno, F., Kerrich, R., 2013b. Hydrothermal nickel deposits: secular variation and diversity. Ore Geol. Rev. 52, 1–3.
Grant, J.A., 1986. The isocon diagram–a simple solution to Greens' Equation for metasomatic alteration. Econ. Geol. 81, 1976–1982.
Heinrich, C.A., Candela, P.A., 2014. Fluids and ore formation in the Earth's crust. In: In: Holland, H.D., Turekian, K.K. (Eds.), Treatise on Geochemistry 2E. Elsevier, Amsterdam, pp. 1–28.
Hou, J., 1992. Nickel mineralization in the Heimulin-Chadian ultramafic suites in Shaanxi Province. Metal. Geol. 10, 16–19 (in Chinese).
Jiang, X.D., Wei, G.F., Nie, J.T., 2010. Jianchaling nickel deposit: magmatic or hydrothermal origin? Min. Dep. 29, 1112–1124 (in Chinese with English abstract).
Johnson, J.W., Oelkers, E.H., Helgeson, H.C., 1992. SUPCRT92: a software package for calculating the standard molal thermodynamic properties of minerals, gases, aqueous species, and reactions from 1 to 5000 bar and 0 to 1000 & #xB0;C. Comput. Geosci. 18, 899–947.
Keays, R.R., Jowitt, S.M., 2013. The Avebury Ni deposit, Tasmania: a case study of an unconventional nickel deposit. Ore Geol. Rev. 52, 4–17.
Kelemen, P.B., Matter, J., Streit, E.E., Rudge, J.F., Curry, W.B., Blusztajn, J., 2011. Rates and mechanisms of mineral carbonation in peridotite: natural processes and recipes for enhanced, in situ CO_2 capture and storage. Annu. Rev. Earth Planet. Sci. 39, 545–576.
Le Vaillant, M., Barnes, S.J., Fiorentini, M.L., Santaguida, F., Törmänen, T., 2016. Effects of hydrous alteration on the distribution of base metals and platinum group elements within the Kevitsa magmatic nickel sulphide deposit. Ore Geol. Rev. 72, 128–148.
Li, J., Dong, W.C., Guo, L.H., Zhu, W., Chen, Y., Zheng, X.G., 2014. The ore control factors and the ore-prospecting indicators of the Jianchaling nickel ore in Shaanxi Province. Northwestern Geol. 47, 54–61 (in Chinese with English abstract).
Liu, W.H., Migdisov, A., Williams-Jones, A., 2012. The stability of aqueous nickel(II) chloride complexes in hydrothermal solutions: results of UV–Visible spectroscopic experiments. Geochim. Cosmochim. Acta 94, 276–290.
Loukola-Ruskeeniemi, K., Lahtinen, H., 2013. Multiphase evolution in the black-shale-hosted Ni–Cu–Zn–Co deposit at Talvivaara, Finland. Ore Geol. Rev. 52, 85–99.
Lu, S., Yan, D.P., Wang, Y., Gao, J.F., Qi, L., 2010. Geochemical and geochronological constrains on the Mashan and Mupi plutons in the South Qinling orogenic belt: implications for tectonic nature of the Bikou Terrane. Acta Petrol. Sin. 26, 1889–1901 (in Chinese with English abstract).
McDonough, W.F., Sun, S.S., 1995. The composition of the Earth. Chem. Geol. 120, 223–253.
Melekestseva, I.Y., Zaykov, V.V., Nimis, P., Tret'yakov, G.A., Tessalina, S.G., 2013. Cu–(Ni–Co–Au)-bearing massive sulfide deposits associated with mafic–ultramafic rocks of the Main Urals Fault, South Urals: geological structures, ore textural and mineralogical features, comparison with modern analogs. Ore Geol. Rev. 52, 18–36.
Molnár, F., Watkinson, D.H., Everest, J.O., 1999. Fluid-inclusion characteristics of hydrothermal Cu–Ni–PGE veins in granitic and metavolcanic rocks at the contact of the Little Stobie deposit, Sudbury, Canada. Chem. Geol. 154, 1279–1301.
Naldrett, A.J., 2004. Magmatic Sulfide Deposits: Geology, Geochemistry and Exploration. Springer, Heidelberg p. 727.
Pirajno, F., González-Álvarez, I., 2013. A re-appraisal of the Epoch nickel sulphide deposit, Filabusi Greenstone Belt, Zimbabwe: a hydrothermal nickel mineral system? Ore Geol. Rev. 52, 58–65.
Qiu, T., Zhu, Y.F., 2015. Geology and geochemistry of listwaenite-related gold mineralization in the Sayi gold deposit, Xinjiang, NW China. Ore Geol. Rev. 70, 61–79.
Seward, T.M., Williams-Jones, A.E., Migdisov, A.A., 2014. The chemistry of metal transport and deposition by ore-forming hydrothermal fluids. In: In: Holland, H.D., Turekian, K.K. (Eds.), Treatise on Geochemistry 2E. Elsevier, Amsterdam, pp. 29–57.
Simon, G., Essene, E.J., 1996. Phase relations among selenides, sulfides, tellurides, and oxides: I. thermodynamic properties and calculated equilibria. Econ. Geol. 91, 1183–1208.
Sun, W.D., Li, S.G., Chen, Y.D., Li, Y.J., 2002. Timing of synorogenic granitoids in the South Qinling, Central China: constraints on the evolution of the Qinling-Dabie orogenic belt. J. Geol. 110, 457–468.
Teir, S., Kuusik, R., Fogelholm, C., Zevenhoven, R., 2007. Production of magnesium carbonates from serpentinite for long-term storage of CO_2. Int. J. Miner. Process. 85, 1–15.
Tian, Y., Etschmann, B., Liu, W., Borg, S., Mei, Y., Testemale, D., O'Neill, B., Rae, N., Sherman, D.M., Ngothai, Y., Johannessen, B., Glover, C., Brugger, J., 2012. Speciation of nickel(II) chloride complexes in hydrothermal fluids: in-situ XAS study. Chem. Geol. 334, 345–363.
Ulrich, M., Muñoz, M., Guillot, S., Cathelineau, M., Picard, C., Quesnel, B., Boulvais, P., Couteau, C., 2014. Dissolution–precipitation processes governing the carbonation and silicification of the serpentinite sole of the New Caledonia ophiolite. Contrib. Miner. Petrol. 167, 1–19.
Vaughan, D.J., Craig, J.R., 1978. Mineral chemistry of metal sulfides. Cambridge University Press, London 261-314.
Waldner, P., Pelton, A.D., 2004. Critical thermodynamic assessment and modelling of the Fe–Ni–S system. Metal. Mater. Trans. B 35, 897–907.
Waldner, P., 2009. Thermodynamic modelling of violarite. J. Chem. Thermodyn. 41, 171–174.
Wang, R.T., He, Y., Tang, Z.L., Wang, D.S., Liu, M.W., 2002. Study on minor elements geochemistry in Jianchaling large cobalt-bearing sulfide nickel deposit. Min. Dep. 21, 1041–1044 (in Chinese).
Wang, R.T., He, Y., Wang, D.S., Liu, M.W., 2003. Re–Os isotope age and its application to the Jianchaling nickel–copper sulfide deposit, Lueyang, Shaanxi Province. Geol. Rev. 49, 205–211 (in Chinese with English abstract).
Wang, R.T., Mao, J.W., Ren, X.H., Wang, J.Y., Wang, X.H., 2005. Ore composition and hosting condition in the Jianchaling sulfide nickel deposit, Shaanxi Province. J. Earth Sci. Environ. 27, 34–38 (in Chinese with English abstract).
Wang, W., Liu, S.W., Feng, Y.G., Li, Q.G., Wu, F.H., Wang, Z.Q., Wang, R.T., Yang, P.T., 2012. Chronology, petrogenesis and tectonic setting of the Neoproterozoic Tongchang dioritic pluton at the northwestern margin of the Yangtze Block: Constraints from geochemistry and zircon U-Pb–Hf isotopic systematics. Gondwana Res. 22, 699–716.
Wang, X., Tang, R.Y., Li, S., Li, Y.X., Yang, M.J., Wang, D.S., Guo, J., Liu, P., Liu, R.D., Li, W.Q., 1996. Qinling Orogeny and Metallogenesis. In: Metallurgical Industry Press, Beijing, pp. 12–31 (in Chinese with English abstract).
Xia, L.Q., Xia, Z.C., Xu, X.Y., Li, X.M., Ma, Z.P., 2007. Petrogenesis of the Bikou Group volcanic rocks. Earth Sci. Front. 14, 84–101 (in Chinese with English abstract).
Xiao, L., Zhang, H.F., Ni, P.Z., Xiang, H., Liu, X.M., 2007. LA-ICP-MS U-Pb zircon geochronology of early Neoproterozoic mafic–intermediate intrusions from NW margin of the Yangtze Block, South China: implication for tectonic evolution. Precambr. Res. 154, 221–235.
Xu, L.G., Lehmann, B., Mao, J.W., 2013. Seawater contribution to polymetallic Ni–Mo–PGE–Au mineralization in Early Cambrian black shales of South China: evidence from Mo isotope, PGE, trace element, and REE geochemistry. Ore Geol. Rev. 52, 66–84.
Yang, L.Q., Deng, J., Qiu, K.F., Ji, X.Z., Santosh, M., Song, K.R., Song, Y.H., Geng, J.Z., Zhang, C., Hua, B., 2015. Magma mixing and crust–mantle interaction in the Triassic monzogranites of Bikou Terrane, central China: constraints from petrology, geochemistry, and zircon U-Pb–Hf isotopic systematics. J. Asian Earth Sci. 98, 320–341.
Zaccarini, F., Garuti, G., 2008. Mineralogy and chemical composition of VMS deposits of northern Apennine ophiolites, Italy: evidence for the influence of country rock type on ore composition. Mineral. Petrol. 94, 61–83.
Zhang, B.R., Chen, D.X., Hu, Y.K., 1986. The geochemical study on ore-formation and ore-metamorphism process of Jianchaling nickel deposit in Lueyang, Shaanxi Province. Earth Sci. 11, 351–365 (in Chinese with English abstract).
Zhang, H.F., Xiao, L., Zhang, L., 2007. Geochemical and Pb–Sr–Nd isotopic compositions of Indosinian granitoids from the Bikou block, northwest of the Yangtze plate: constraints on petrogenesis, nature of deep crust and geodynamics. Sci. China, Ser. D Earth Sci. 50, 972–983.
Zhang, X., Xu, X.Y., Song, G.S., Wang, H.L., Chen, J.L., Li, T., 2010. Zircon LA-ICP-MS U-Pb dating and significance of Yudongzi Group deformation granite from Lueyang area, western Qinling, China. Geol. Bull. China 29, 510–517 (in Chinese with English abstract).
Zhang, Z.Q., Zhang, G.W., Tang, S.H., Wang, J.H., 2001. On the age of metamorphic rocks of the Yudongzi Group and the Archean crystalline basement of the Qinling Orogen. Acta Geol. Sin. 75, 198–204 (in Chinese with English abstract).